CHAPTER 4

Compact Ultra-wideband Bandpass Filter with Improved Performance Using Defected Ground Structure-based Lowpass Filter

4.1 Introduction

Ultra-wideband (UWB) technology has great potential in the development of various modern transmission systems, for instance, through-wall imaging, medical imaging, vehicular radar, indoor and hand-held UWB systems [FCC (2002)]. UWB bandpass filter (BPF) is one of the key components in UWB systems. To satisfy the FCC's requirements as portrayed in [FCC (2002)], a preferred UWB BPF should have good selectivity, uniform group delay and low insertion loss over its passband. In addition to these characteristics, the filter should be very compact in size with good out-of-band rejection to meet the growing demand for modern UWB technology.

Lots of UWB BPFs have been reported in the literature [Ishida and Araki (2004), Yang *et al*. (2011), Wang *et al*. (2005), Hu *et al*. (2006), Zhu *et al*. (2005), Yao *et al*. (2009), Chu *et al*. (2011), Li *et al*. (2015), Jhariya *et al*. (2015), Kumar *et al*. (2016), Zhang *et al*. (2016), Ahmed and Virdee (2013), Gomez-Garcia and Alonso (2006), Yang *et al*. (2007), Ghatak *et al*. (2011), Sarkar *et al*. (2012), Fallahzadeh and Tayarani (2010), Taibi *et al*. (2015)]. However, the reported UWB BPFs need improvement in terms of size, out-of-band performance and/or selectivity so that they can find potential applications in UWB systems including modern UWB communication systems.

Further, in order to improve out-of-band performance for a compact size filter, several approaches are reported in the literature [Garcia-Garcia *et al*. (2006), Wong and Zhu (2007)], [Gong *et al*. (2008)] to suppress the harmonic response. In [Gao *et al*.

(2008), Wei *et al*. (2008), Yang *et al*. (2008), Song *et al*. (2014)], defected ground structures (DGSs) are used to suppress spurious response. For obtaining wide upper stopband, three pairs of tapered DGSs are studied in [Song *et al*. (2014)]. In the filter reported in [Song *et al*. (2014)], upper stopband is extended up to 30 GHz with attenuation level greater than or equal to 15 dB only and size of the filter is also large. Hence, scope still exists for further improvement in the performance of UWB BPFs reported in the literature.

In this chapter, a compact UWB BPF having sharp roll-off, low insertion loss and improved upper stopband performance with highly suppressed unwanted harmonics is described. The proposed filter uses modified multi-mode resonator (MMR), open- as well as short-circuited stubs at input and output ports, and a DGS-based lowpass filter (LPF). The modified MMR consists of meandered coupled-lines, stepped-impedance and open-circuited stubs along with coupled-line sections. To obtain the wide stopband for compact size filter, DGS-based LPF is used. The LPF was realized using four non-uniform cascaded configuration of DGS units where each DGS unit is formed by cascading three isosceles U-shaped DGSs. Further, DGS-based LPF was analysed through *RLC* equivalent circuit model and the theoretical results were verified through simulation and measurement. Finally, simulation and experimental studies of the proposed compact UWB BPF were carried out. Ansys high frequency structure simulator (HFSS) software was used for the numerical simulation study. Roger RT/duroid 5880 dielectric substrate ($\varepsilon_r = 2.2$, $\tan\delta = 0.0009$ and thickness = 0.787 mm) was used for simulation and experimental studies.

4.2 Design and Study of the Multi-mode Resonator (MMR)-based Ultra-wideband (UWB) Bandpass Filter (BPF)

4.2.1 Investigation of the MMR-based UWB BPF

The MMR are used to make compact BPFs. MMRs have closely spaced resonant frequencies, all of which can constitute the passband. An N^{th} order filter employing single mode resonators requires N number of resonators. If an N-mode resonator is used instead, only one resonator is needed. This reduces the size of the filter by a factor of N. To obtain the compact size UWB BPF, the basic idea for using MMR in realizing UWB BPF is taken from [Zhang *et al*. (2016)]. Figure 4.1 shows the geometry of the MMR. The MMR consists of a pair of open-circuited stubs and three pairs of coupled-line sections. For obtaining the resonant modes of MMR, coupling analysis was carried out by considering two coupling conditions: weak and strong couplings. Further, in order to design the compact UWB BPF, the MMR has been used. Figure 4.2 shows the geometry of the MMR-based UWB BPF. In order to cover the UWB frequency range of 3.1 – 10.6 GHz, the coupling length l_c play an important role. Through proper tuning of coupling length l_c, desired frequency range can be obtained by adjusting resonant frequencies. The two pairs of open- and short-circuited stubs at the input/output ports are responsible for improving the passband impedance matching of the filter to some extent and passband selectivity due to the creation of transmission zeros [Wang *et al*. (2012)]. Figure 4.3 shows the simulated magnitude of transmission coefficient $|S_{21}|$-frequency characteristic of the filter for three different values of coupling length 'l_c'. It is to be noted that for two weak coupling cases with l_c = 1 and 2 mm, four resonances corresponding to peak $|S_{21}|$ values appear at the frequencies of 4.54, 7.15, 9.27, and 10.74 GHz. As l_c increases from 1 to 2 mm, the $|S_{21}|$ curve moves upward. As l_c increases further to 7.4 mm, which is the optimised value for strong coupling, an almost

flat frequency response for $|S_{21}|$ close to the 0 dB-line is obtained for the filter over the desired UWB passband.

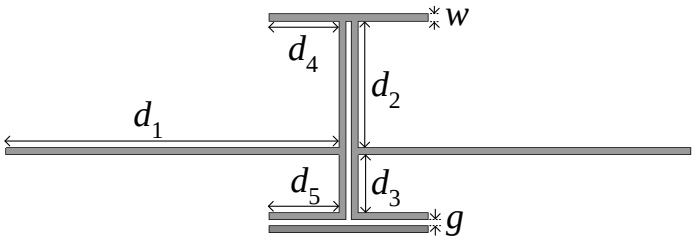

Figure 4.1: Geometry of the MMR.

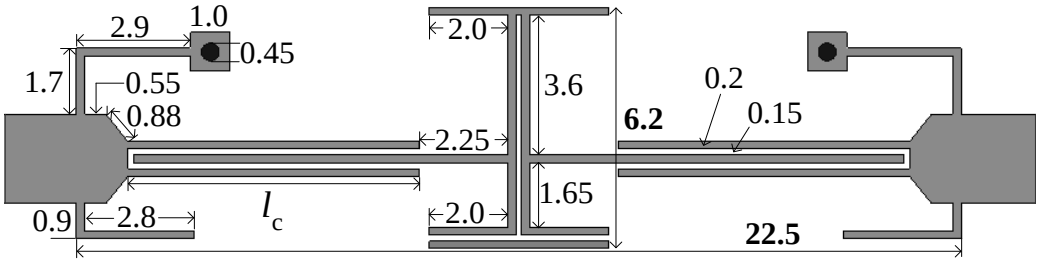

Figure 4.2: Geometry of the MMR-based UWB BPF with optimized dimensions (all dimensions are in millimeter).

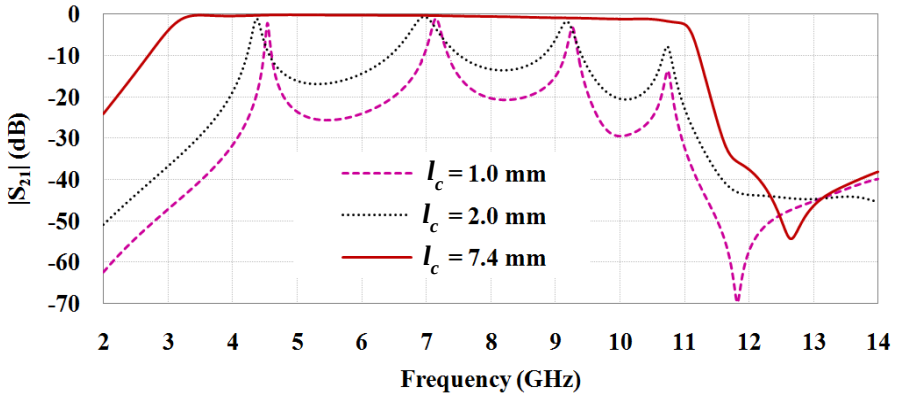

Figure 4.3: Simulated variations of $|S_{21}|$ of MMR-based UWB BPF with frequency for different values of coupling length l_c.

4.2.2 Equivalent Circuit of the MMR-based UWB BPF

The equivalent circuit model of the MMR is shown in Figure 4.4. The modelling of the structure is done by considering four resonant modes of the MMR which appear at the frequencies of 4.54 (f_1), 7.15 (f_2), 9.27 (f_3), and 10.74 (f_4) GHz in Figure 4.3. These

resonant modes are obtained through the coupling analysis of the MMR. These four resonant modes can be divided into two frequency ranges - lower and higher. The upper half and lower half of the MMR equivalent circuit are applicable for lower and higher frequency ranges respectively. Lower frequency range contains the frequencies f_1 and f_2 where response peaks are obtained. The higher frequency range includes the frequencies f_3 and f_4, where again response peaks are achieved. The expressions for the frequencies of individual peaks are given by [Ryder (1994)]

$$f_1 = f_r^{'}\left(1-\frac{1}{2}\sqrt{k^{'2}-\frac{1}{Q_1Q_2}}\right) \tag{4.1}$$

$$f_2 = f_r^{'}\left(1+\frac{1}{2}\sqrt{k^{'2}-\frac{1}{Q_1Q_2}}\right) \tag{4.2}$$

$$f_3 = f_r^{''}\left(1-\frac{1}{2}\sqrt{k^{''2}-\frac{1}{Q_3Q_4}}\right) \tag{4.3}$$

$$f_4 = f_r^{''}\left(1+\frac{1}{2}\sqrt{k^{''2}-\frac{1}{Q_3Q_4}}\right) \tag{4.4}$$

where $f_r^{'}$ and $f_r^{''}$ are the resonant frequencies, and $k^{'}$ and $k^{''}$ are the coupling coefficients of the coupled parallel resonant circuits appearing in upper half and lower half of the MMR equivalent circuit respectively, Q_1, Q_2, Q_3, and Q_4 are the quality factors of the parallel resonant circuits consisting of R_2-L_2-C_2, R_3-L_3-C_3, R_5-L_5-C_5, and R_6-L_6-C_6 respectively.

The parallel resonant circuits of the upper half and lower half of the MMR equivalent circuit operate as overcoupled circuits in which coupling is provided through capacitors C_{c1} and C_{c2} respectively. For the two coupled resonant circuits to operate as overcoupled circuits, the following conditions should be satisfied:

$$k' > \frac{1}{\sqrt{Q_1 Q_2}}, \text{ and } k'' > \frac{1}{\sqrt{Q_3 Q_4}}$$

The series and parallel circuits of the upper half of the MMR equivalent circuit consisting of R_1-L_1-C_1, and R_2-L_2-C_2 as well as R_3-L_3-C_3 resonate at a frequency f_r' midway between the frequencies f_1 and f_2, where peaked responses are obtained due to overcoupling between parallel resonant circuits in lower frequency range. Similarly, the series and parallel circuits of the lower half of the MMR equivalent circuit consisting of R_4-L_4-C_4, and R_5-L_5-C_5 as well as R_6-L_6-C_6 resonate at a frequency f_r'' midway between the frequencies f_3 and f_4 where peaked responses are obtained due to overcoupling between parallel resonant circuits in higher frequency range. The coupling capacitors C_{c1} and C_{c2} are responsible for making the corresponding parallel resonant circuits as overcoupled circuits to achieve broad bandwidth. The responses of upper half and lower half of the MMR equivalent circuit overlap each other due to the inter-coupling of overcoupled resonant circuits. This results in overall wideband response as shown in Figure 4.3.

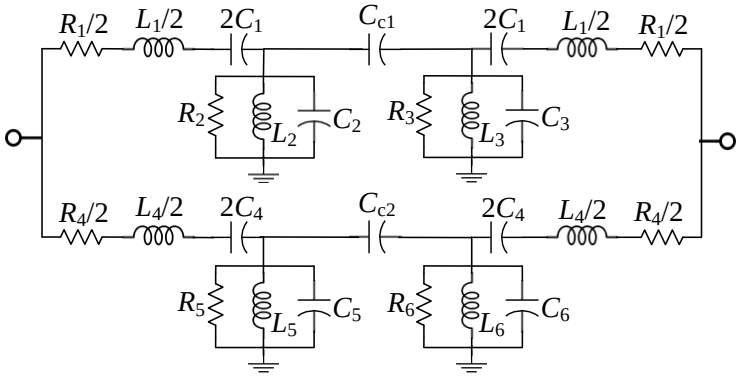

Figure 4.4: Equivalent circuit model of the MMR.

The equivalent circuit model of the MMR-based UWB BPF is shown in Figure 4.5. In order to couple the power from input port to the MMR, effective coupling should take place. The coupling capacitor C_{c3} is used to effectively couple the MMR circuit to the input/output port. The value of coupling capacitor C_{c3} should be taken in such a way

that the reactance due to coupling capacitor is very less as compared with the input/output impedance of the filter. The short- and open-stubs connected at the input/output ports which are responsible for achieving passband selectivity due to the creation of transmission zeros, are represented by parallel and series resonant circuits respectively. The L_7-C_7 parallel resonant circuit connected in series corresponds to short-circuit stub which resonates at ~11.5 GHz. The L_8-C_8 series resonant circuit connected in shunt corresponds to open-circuit stub which resonates at ~14 GHz.

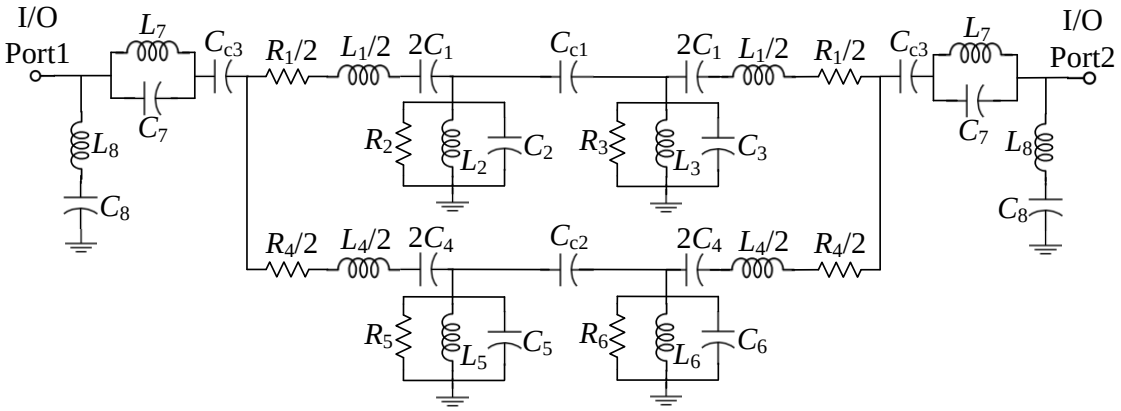

Figure 4.5: Equivalent circuit model of the MMR-based UWB BPF.

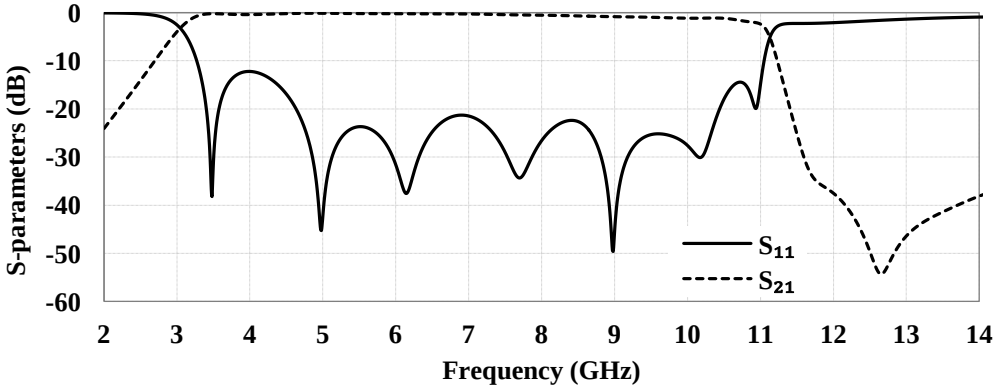

Figure 4.6: Simulated variation of magnitudes of S-parameters of the MMR-based UWB BPF with frequency.

4.2.3 Results and Discussion of the MMR-based UWB BPF

The simulated S-parameters of the MMR-based UWB BPF with frequency are shown in Figure 4.6. From Figure 4.6, it can be observed that the 3-dB passband frequency range

of the BPF is 3 – 11 GHz with low insertion loss. The maximum value of insertion loss at a mid-band frequency of the filter passband is found to be 0.27 dB. Figure 4.7 shows the simulated variation of the group delay of the MMR-based UWB BPF with frequency. From Figure 4.7, it is observed that in the passband, simulated values of group delay vary over the range 0.3 – 1.0 ns.

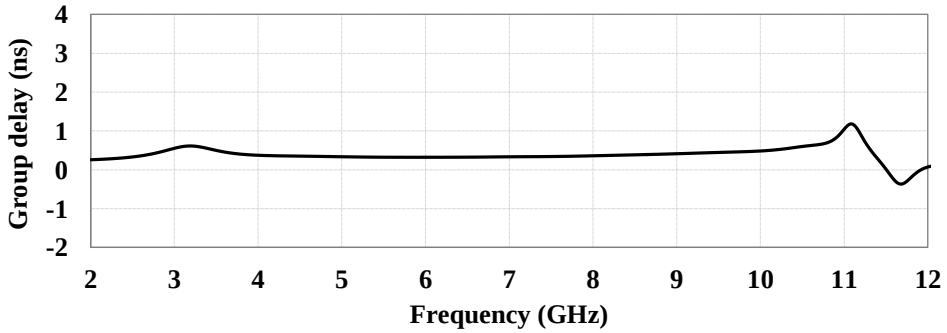

Figure 4.7: Simulated variation of group delay of the MMR-based UWB BPF with frequency.

4.3 Design and Investigation of the Modified MMR-based UWB BPF

4.3.1 Design of the Modified MMR-based UWB BPF

In order to miniaturize the aforesaid design of MMR-based UWB BPF, the MMR is modified. The modified MMR consists of meandered coupled-lines (MCLs), stepped-impedance (SI) stubs, open-circuited stubs and parallel coupled-line sections. The significant reduction in filter size (~41%) is achieved as compared to the filter shown in Figure 4.1 due to the use of MCLs but the price is paid in terms of increased input reflection in the passband. Owing to mutual coupling between MCLs, effective values of capacitances and inductances representing the MCLs and hence corresponding reactances will change. Thus, to nullify the reactances generated due to the MCLs, SI stubs of optimized dimensions are inserted at proper locations of the filter structure to improve impedance matching in the passband. It is worth mentioning that open- and

short-circuited stubs at input and output ports of the filter are also responsible for improving the passband selectivity and impedance matching of the filter to some extent. The modified MMR-based UWB BPF having optimized dimensions (obtained through numerical simulation) is shown in Figure 4.8. Table 4.1 shows the simulated design parameters with optimised dimensions of the proposed modified MMR-based UWB BPF. The physical area of the modified MMR-based UWB BPF is 14 mm × 5.9 mm. Further, prototype of the modified MMR-based UWB BPF with SI-stubs was fabricated (shown in inset view of Figure 4.11) on RT/duroid 5880 dielectric substrate (ε_r = 2.2, tanδ = 0.0009 and thickness = 0.787 mm) and parameters of interest: *S*-parameter and group delay as functions of frequency were measured over the frequency range 2 – 18 GHz in order to validate the respective numerical simulation results.

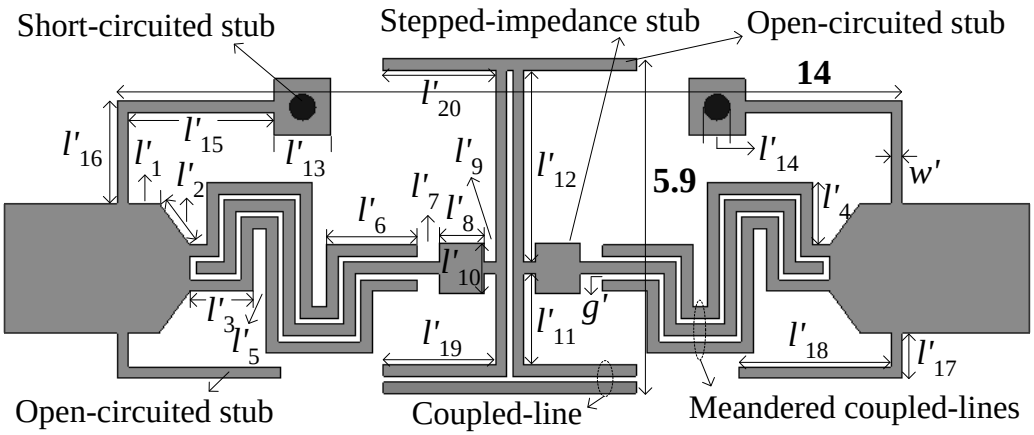

Figure 4.8: Geometry of the modified MMR-based UWB BPF.

Table 4.1: The optimised parameters of the modified MMR-based UWB BPF (all dimensions are in millimeter).

l'_1 = 0.55	l'_2 = 0.93	l'_3 = 1.1	l'_4 = 1.1	l'_5 = 0.25	l'_6 = 1.61
l'_7 = 0.39	l'_8 = 0.8	l'_9 = 0.2	l'_{10} = 0.9	l'_{11} = 1.6	l'_{12} = 3.4
l'_{13} = 1.0	l'_{14} = 0.46	l'_{15} = 2.6	l'_{16} = 1.8	l'_{17} = 0.8	l'_{18} = 2.7
l'_{19} = 1.99	l'_{20} = 2.0	g' = 0.11	w' = 0.2	–	–

4.3.2 Equivalent Circuit of the Modified MMR-based UWB BPF

The equivalent circuit model of the modified MMR-based UWB BPF is shown in Figure 4.9, in which equivalent circuit model of the MMR-based UWB BPF shown in Figure 4.5 is modified to incorporate the effect of the use of SI stubs in the modified BPF. In order to nullify the reactance generated due to the MCLs for impedance matching, the SI-stubs are used. The SI-stub corresponding to a short length of low-impedance line terminated at either end by relatively high impedance, is represented by a T-equivalent circuit with the circuit parameters L_9-C_9 [Hong and Lancaster (2001)]. The stub equivalent circuits are included in the equivalent circuit model of the modified MMR-based UWB BPF shown in Figure 4.9.

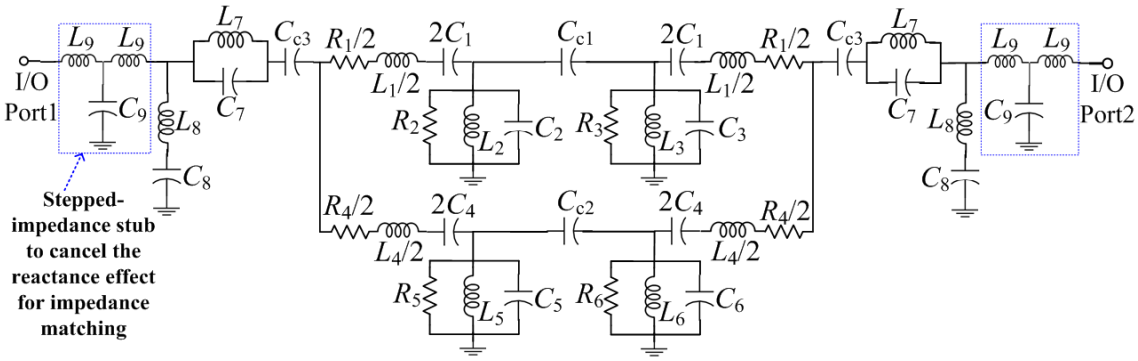

Figure 4.9: Equivalent circuit model of the modified MMR-based UWB BPF.

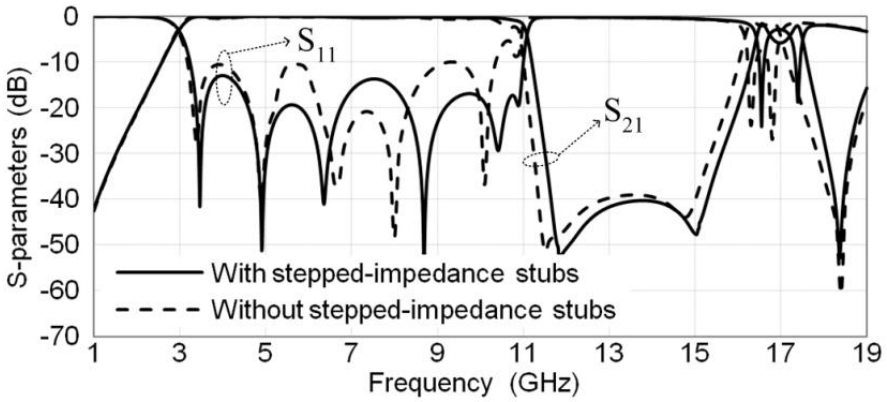

Figure 4.10: Simulated variations of magnitudes of S-parameters of modified MMR-based UWB BPF with and without SI stubs versus frequency.

4.3.3 Results and Discussion

In order to understand the effect of SI-stubs for impedance matching, S-parameters of the modified MMR-based UWB BPF with and with SI-stubs have been studied. Figure 4.10 shows simulated *S*-parameter-frequency characteristics of modified MMR-based UWB BPF with and without SI-stubs. It can be observed from Figure 4.10 that impedance matching improves in the presence of SI-stubs. It is also observed from Figure 4.10 that frequency range of passband is 3 – 11 GHz with low insertion loss, good selectivity and better impedance matching for modified MMR-based UWB BPF with SI-stubs. Further, it is discerned that undesired response is observed at or near 17 GHz with/without SI stubs. The experimental characteristics of the fabricated filter are shown in Figure 4.11 along with corresponding numerical simulation results. The simulated and experimental parameter values of the modified MMR-based UWB BPF extracted from Figure 4.11 are given in Table 4.2. It can be seen from Table 4.2 that experimental results for modified MMR-based UWB BPF are nearly in agreement with the respective simulation results. The deviation in the results may be due to finite SMA connector losses as well as fabrication and measurement errors.

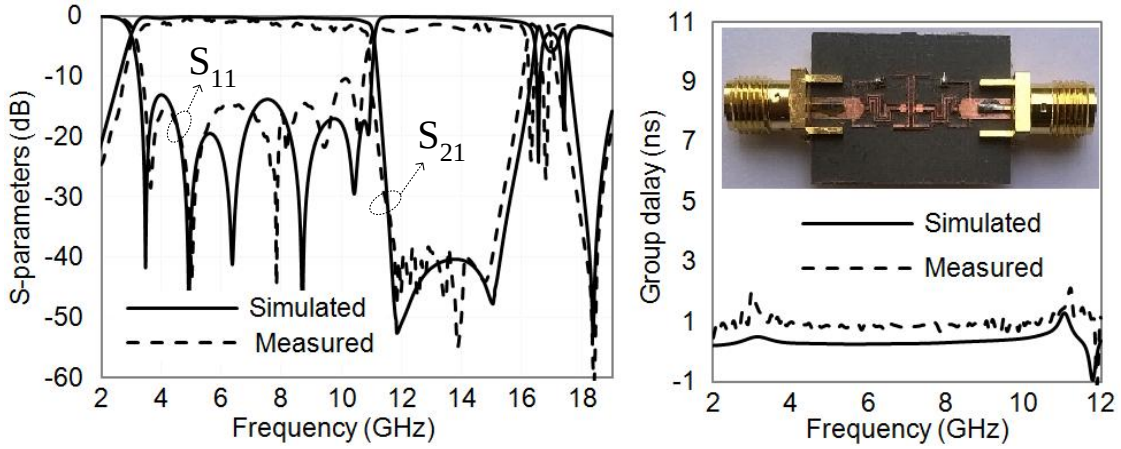

Figure 4.11: Simulated and measured results for the modified MMR-based UWB BPF (inset view shows the fabricated prototype of the filter).

Since the unwanted harmonic response is observed at and around 17 GHz, it should be suppressed in order to achieve improved out-of-band performance/wide stopband with high unwanted harmonic rejection capability. Hence, to achieve the compact UWB BPF with improved out-of-band performance, a new compact DGS-based LPF is designed and integrated with the modified MMR-based UWB BPF.

Table 4.2: Simulation and measured results of the modified MMR-based UWB BPF.

	3-dB bandwidth (GHz)	Stopband (GHz), attenuation (dB)	IL*	GD*
Simulated	3.0–11.0	Upto 15.5, 42	0.5 dB	0.5 ns
Measured	3.05–10.9	Upto 15.5, 38	1.1 dB	1.0 ns

*Insertion loss (IL) and group delay (GD) at mid frequency of UWB passband

4.4 Defected Ground Structure (DGS)-based Lowpass Filter (LPF)

4.4.1 Introduction

DGS realized by etching a defected pattern in the ground plane can provide bandgap characteristics from its resonance property [Kim *et al*. 2000] and find potential application in microwave circuits to suppress spurious responses and reduce circuit size [Ahn *et al*. 2001]. Various shapes of DGSs viz. dumbbell-shaped [Kim *et al*. (2000), Ahn *et al*. (2001), Lim *et al*. (2002), Liu *et al*. (2004), Mollah *et al*. (2005)], rectangular slot and metal-loaded slots [Zhang and Mansour (2004)], cross-shaped [Chen *et al*. (2006)], complementary split-ring resonator shaped [Weng *et al*. (2008)], H-shaped [Mandal and Sanyal (2006)], elliptic-shaped [Chen *et al*. (2009)], fork-shaped [Yu *et al*. (2009)], modified Pi-shaped [Moyra *et al*. (2010)], interdigital-shaped [Liu *et al*. (2015)], U-shaped and V-shaped DGSs [Woo *et al*. (2006), Ting *et al*. (2006)] are described in the literature which demonstrates their technical viability and applications. The large defected ground area employed in a filter can degrade its performance. The

reported DGSs need improvement either in terms of defected ground area and/or performance. In [Ting *et al*. (2006)], double equilateral U-shaped DGS (UDGS) unit is reported which provide double attenuation poles and has less number of degrees of freedom to control the attenuation pole frequencies by varying its dimensions.

The bandgap characteristics of a DGS, which is mainly ascribed by a finite number of attenuation poles opened the door for the design of lowpass filters (LPFs). In [Ahn *et al*. (2001)], conventional dumbbell-shaped DGSs with microstrip line having T-junction and cross-junction type open stubs have been used to design an LPF. The LPF using dumbbell-shaped DGS patterns and the compensated microstrip line is reported in [Lim *et al*. (2002)]. In [Vala *et al*. (2017)], dumbbell-shaped DGS has been used for the design of an LPF. The LPFs reported in [Ahn *et al*. (2001), Lim *et al*. (2002), Vala *et al*. (2017)] have large defected ground area and need improvement in the passband and stopband performances. In [Mollah *et al*. (2005)], non-uniform dumb-bell shaped DGS and photonic-bandgap (PBG) structures have been used to improve the characteristics of LPF. The non-uniform distribution of dumbbell-shaped DGS and PBG structures provides better performance as compared with uniform distribution. But large defected ground area employed in a filter can degrade its performance. In [Mandal and Sanyal (2006)], H-headed dumbbell-shape DGS with microstrip line having cross-junction open stub is used for the design of an LPF. The periodic arrangement of three cascaded square complementary split-ring resonator (CSRR) DGS units are used in the design of an LPF in [Weng *et al*. (2008)]. In [Chen *et al*. (2009)], elliptic-shaped DGS cells with microstrip line having H-shaped open stubs have been used to design an LPF to achieve strong coupling with good stopband performance. Three cascaded DGS units incorporating fork-shaped DGSs [Yu *et al*. (2009)] and a modified Pi-shaped DGS [Moyra *et al*. (2010)] with compensated microstrip line have been used in the design of

LPFs [Yu *et al*. (2009), Moyra *et al*. (2010)]. The design of LPFs based on three unit cells of cross-shaped DGSs [Chen *et al*. (2006)], interdigital-shaped DGS [Liu *et al*. (2015)] and two open loops ring-shaped slot based DGS unit [Fu and Yu (2016)] is reported. Dumbbell-shaped slots have been introduced in the middle of DGSs for improving the stopband performance of LPF [Zhou *et al*. (2011)]. Periodic double radial stubs (DRSs) and fan-shaped DGSs have been used for the design of LPF in [Ertay *et al*. (2016)]. The design of reported LPF is intricate, and it has larger defected ground area. The LPFs reported in the literature need improvement either in terms of size or passband and stopband performances or both. A microstrip LPF using uniform and non-uniform metal-loaded slots in the ground plane is reported in [Zhang and Mansour (2004)]. In [Ting *et al*. (2006)], double equilateral UDGS unit connected in non-uniform cascaded configuration has been used to design an LPF. It is reported in [Zhang and Mansour (2004), Ting *et al*. (2006)] that non-uniform cascaded arrangement of the slot in the ground plane provides better performance as compared with the uniform cascaded arrangement. However, reported filters [Zhang and Mansour (2004), Ting *et al*. (2006)] have the scope for further improvement in size as well as passband and stopband performances.

Hence, a compact LPF with wide stopband is proposed which uses a uniform 50 Ω microstrip line along with four non-uniform cascaded DGS units. The proposed filter is simple in structure and does not employ compensated microstrip line, open stub, low-high impedance line, and tee- or cross-junction elements reported in the literature. Each DGS unit, which consists of three isosceles UDGSs, provides three attenuation poles whose frequencies can be controlled by varying the dimensions of individual DGSs. The frequency response of the proposed isosceles UDGS is analysed, and performance comparison of the UDGS and conventional dumbbell- as well as fork-shaped DGSs is

carried out. The proposed single and triple isosceles UDGS(s) in combination with 50 Ω microstrip line are analyzed through equivalent *RLC* circuit models and numerical simulations. The effect of coupling between UDGSs on attenuation pole frequencies is explained by incorporating coupling capacitors in the equivalent circuit model of proposed DGS unit-microstrip line combination and studying circuit response by varying the values of coupling capacitors. Further, *RLC* circuit modelling and analysis of the proposed LPF are carried out using circuit and numerical simulations. The proposed LPF has simulated 3-dB cut-off frequency of 14.2 GHz with stopband extending up to 30 GHz. The overall size of the filter is 14.44 mm × 3.4 mm. The design and optimization of the filter are done using Ansys HFSS numerical simulation software. The designed filter is fabricated and experimentally tested for the variations of reflection coefficient and transmission coefficient versus frequency. The circuit and numerical simulation results are compared among themselves as well as with the respective experimental ones. In addition, performance and dimension based comparison of the proposed LPF with those reported in the literature is presented.

4.4.2 Single Isosceles U-shaped DGS (UDGS)

4.4.2.1 Analysis and Modelling of Single Isosceles U-shaped DGS

The basic idea about the initial geometry of single UDGS is taken from [Ting *et al.* (2006)] in which microstrip LPF with wide stopband is designed using double equilateral UDGSs. In the proposed work, use is made of isosceles UDGSs because of the availability of more degrees of freedom in them to control the dimensions for obtaining desired attenuation pole frequencies. The geometry of single isosceles UDGS placed symmetrically on the ground plane is shown in Figure 4.12(a), where a 50 Ω microstrip line is also seen with the strip conductor and the ground plane placed on

opposite sides of Rogers RT/duroid 5880 substrate having dielectric constant (ε_r) of 2.2 and thickness of 0.787 mm. The name 'isosceles UDGS' stems from the fact that it has two identical side lengths. The middle length of DGS can be same as or different from side lengths as per the requirement of attenuation pole frequency. To obtain the attenuation pole at a particular frequency, maximum power should be consumed by the circuit at that frequency. Hence, the UDGS-microstrip line combination is analyzed in terms of a parallel *RLC* resonant circuit to block the passage of the signal from input to output at or near its resonant frequency. The magnitudes of *S*-parameters for single UDGS of dimensions l_1 = 3.35 mm, l_2 = 2.88 mm, and w = 0.25 mm in combination with microstrip line are estimated at different frequencies using MATLAB software. The equivalent *RLC* circuit parameters of the i^{th} UDGS are extracted using [Woo *et al*. (2006)]:

$$R_i = 2Z_0 \Big/ \sqrt{\left(1/\left|S_{11}\left(f_{0i}\right)\right|^2\right) - \left(2Z_0\left(2\pi f_{0i}C_i - \left(1/\left(2\pi f_{0i}L_i\right)\right)\right)\right)^2} - 1$$
$$L_i = 1/4\pi^2 f_{0i}^2 C_i; \quad C_i = f_{ci}\Big/\left(4\pi Z_0\left(f_{0i}^2 - f_{ci}^2\right)\right) \qquad \text{for } i = 1,2,3 \tag{4.5}$$

where Z_0 is the characteristic impedance of the microstrip line, and f_{ci}, f_{0i} and $|S_{11}(f_{0i})|$ are respectively the 3-dB cut-off frequency, resonant frequency and magnitude of input reflection coefficient at the resonant frequency of i^{th} UDGS. From the numerically simulated scattering parameter-frequency characteristics of i^{th} UDGS obtained through Ansys HFSS software (shown in Figure 4.12(c)), circuit parameters are computed using Equation (4.5). The computed values of circuit parameters are found to be: R_i = 2.7571 kΩ, L_i = 0.34297 nH, and C_i = 0.32684 pF. The values of *S*-parameters for i^{th} UDGS at different frequencies are computed from the equivalent circuit shown in Figure 4.12(b) using MATLAB software, and the results of the circuit model are shown in Figure 4.12(c). From Figure 4.12(c), it is observed that variations of numerically simulated magnitudes of *S*-parameters of i^{th} UDGS with frequency are nearly in agreement with

corresponding characteristics obtained using its equivalent circuit model. It can also be seen from Figure 4.12(c) that single UDGS provides one attenuation pole at 15 GHz.

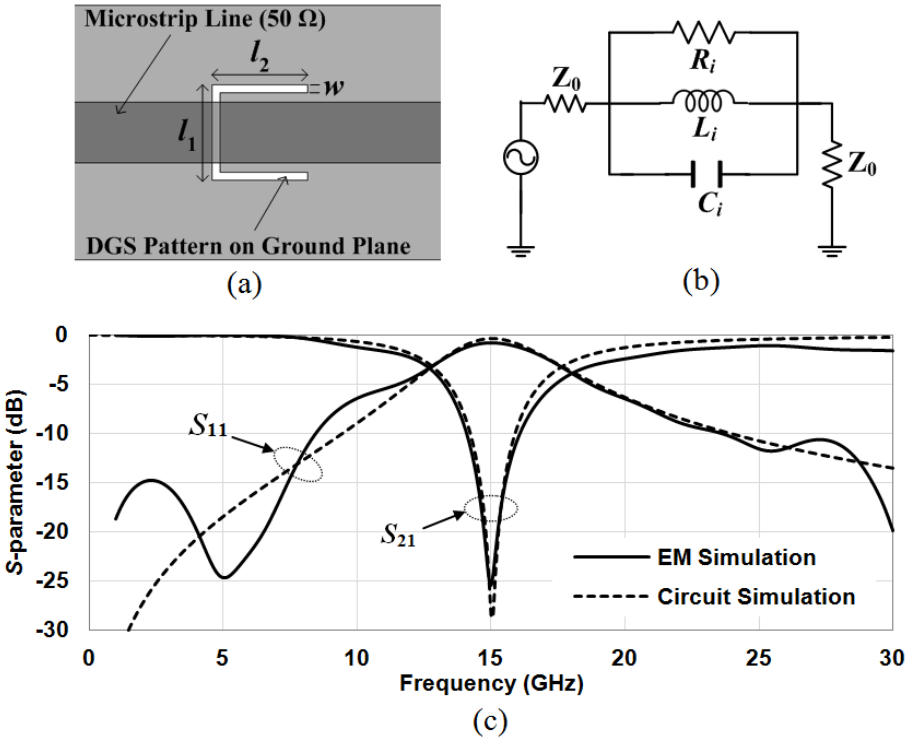

Figure 4.12: (a) Geometry of single UDGS on the ground plane along with 50 Ω microstrip line. (b) The equivalent *RLC* circuit model of single UDGS. (c) The magnitudes of *S*-parameters versus frequency for single UDGS having dimensions l_1 = 3.35 mm, l_2 = 2.88 mm, and w = 0.25 mm.

4.4.2.2 Parametric Study of Single Isosceles U-shaped DGS

The effects of variations in the dimensions of single UDGS on magnitude of S_{21} of single UDGS-microstrip line combination with frequency are explored. Different dimensions of UDGS provide more degrees of freedom to control the attenuation pole frequency. Figure 4.13 shows the results of the parametric study in which side length 'l_2', middle length 'l_1' and slot width 'w' of single UDGS are changed one at a time to observe their effects on the magnitude of S_{21}-frequency characteristic of UDGS-microstrip line combination. Significant variation in resonant frequency of the structure is observed in Figure 4.13 due to change in side length 'l_2' and slot width 'w' while

little change in its resonant frequency is seen by varying middle length 'l_1' while keeping other dimensions of UDGS fixed. As length 'l_1' increases, the separation between two side lengths of UDGS increases which will result in decrease of capacitance C_i of the structure. But on increasing the length 'l_1', inductance L_i of the structure will increase. The increase in structure's inductance L_i dominates over decrease in capacitance C_i with increase in the middle length 'l_1' which results in slight reduction in the resonant frequency (attenuation pole frequency) of the UDGS as per Equation (4.5). As side length 'l_2' of the UDGS increases, the separation between two side lengths remains the same but the area affecting C_i value of the UDGS increases which results in increase of the capacitance C_i. The increase in C_i-value results in the decrease of resonant frequency (attenuation pole frequency) of the UDGS as per Equation (4.5) given earlier. It is worth mentioning here that in view of keeping the overall length of the proposed UDGS small, the 'l_2' value was taken less than 'l_1' value. Figure 4.13(c) shows the variation of $|S_{21}|$ of single UDGS-microstrip line combination with frequency by taking slot width 'w' of the UDGS as a parameter. It can be seen from Figure 4.13(c) that the effect of variation in slot width 'w' on the magnitude of transmission coefficient $|S_{21}|$ of the structure is also significant. As slot width 'w' increases, slot radiation will increase. Simultaneously, the decrease in slot width 'w' value may complicate the structure's fabrication process. Therefore, in order to avoid slot radiation and fabrication complexity, the optimum value of slot width 'w' was chosen as 0.25 mm.

4.4.2.3 Performance Comparison of the Proposed Single Isosceles U-shaped DGS with Dumbbell- and Fork-shaped DGSs

In order to compare the performance of the proposed single cell of isosceles UDGS with conventional dumbbell-shaped DGS reported in [Kim *et al*. (2000), Ahn *et al*. (2001),

Lim *et al*. (2002), Liu *et al*. (2004)] and fork-shaped DGS described in [Yu *et al*. (2009)] whose configurations are shown in Figure 4.14, numerical simulation was performed, and the simulation results are shown in Figure 4.15. It is worth mentioning that identical substrate material–RT duroid 5880 (ε_r = 2.2, tanδ = 0.0009 and thickness = 0.787 mm) were taken in the simulation study for all the DGS shapes considered here. Table 4.3 shows the comparative study of different unit cells of DGSs reported in the literature with the proposed unit cell of DGS. It is apparent from Table 4.3 that the proposed isosceles UDGS is more compact for same resonant frequency and provides higher quality factor as compared with dumbbell- and fork-shaped DGSs. Hence UDGS, which has much better characteristics as compared with dumbbell- and fork-shaped DGSs is chosen for further study.

4.4.3 Triple Isosceles U-shaped DGS (Proposed DGS Unit)

4.4.3.1 Design and Analysis of Triple Isosceles U-shaped DGS

For obtaining wide stopband, the number of attenuation poles has to be increased without sacrificing the size of the structure. Hence, two more UDGSs of smaller dimensions are embedded inside the outer UDGS forming one DGS unit. Figure 4.16(a) shows the geometry of the proposed triple isosceles UDGS unit along with 50 Ω microstrip line. The simulation study was carried out using Ansys HFSS numerical simulation software. The optimized dimensions of the DGS unit obtained through numerical simulation are: l_1 = 3.35 mm, l_2 = 2.88 mm, l_3 = 2.45 mm, l_4 = 2.42 mm, l_5 = 1.55 mm, and l_6 = 1.81 mm. The numerically simulated transmission coefficient $|S_{21}|$-frequency characteristic of the DGS unit-microstrip line combination is shown in Figure 4.16(b). From Figure 4.16(b), it is observed that the structure provides three attenuation poles corresponding to the resonant frequencies of 14.56, 18.75, and 25.98 GHz.

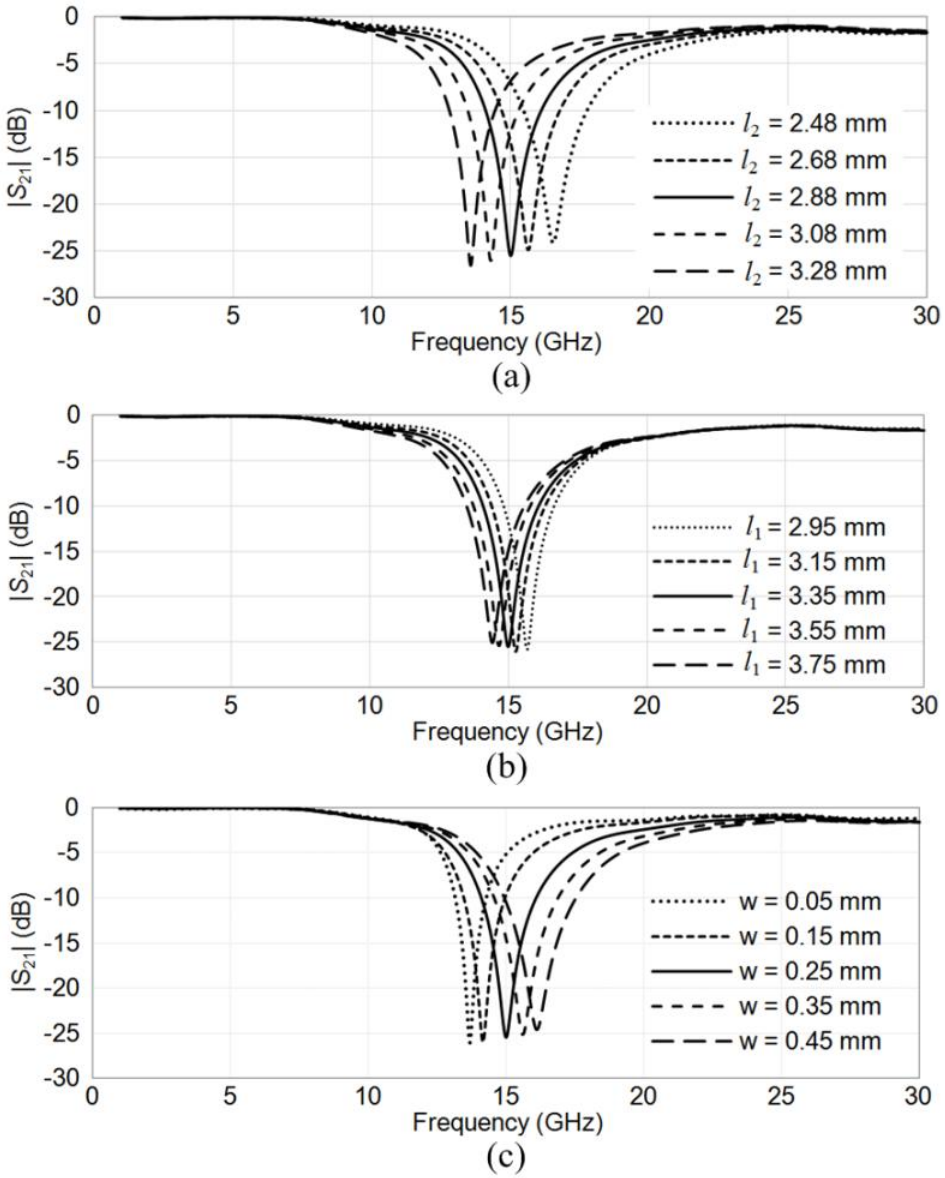

Figure 4.13: Variations of numerically simulated magnitude of S_{21} of single UDGS-microstrip line combination with frequency for different values of (a) 'l_2', (b) 'l_1', and (c) 'w'; keeping other dimensions fixed.

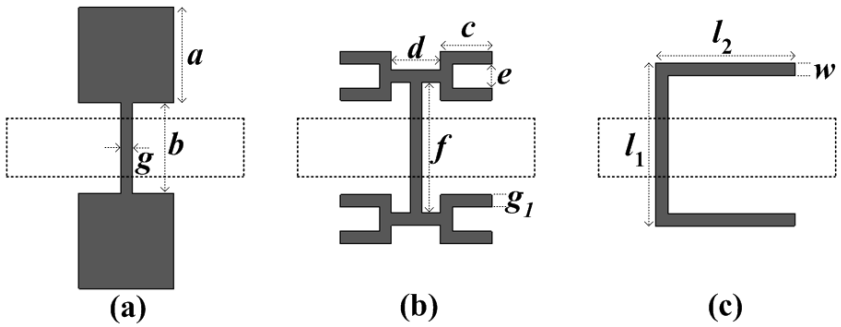

Figure 4.14: Geometries of different DGS configurations (a) Dumbbell-shaped DGS, (b) Fork-shaped DGS, and (c) U-shaped DGS.

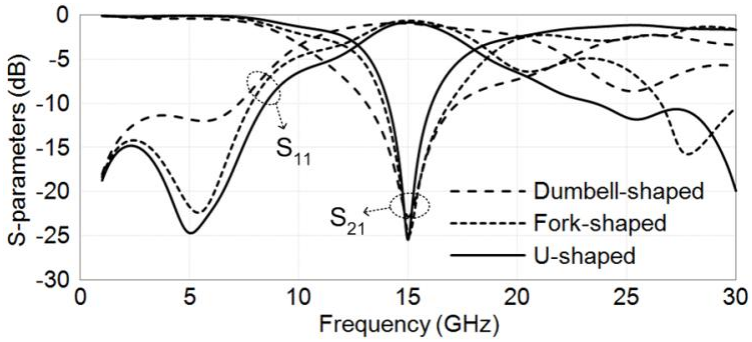

Figure 4.15: Variations of numerically simulated magnitudes of *S*-parameters for different DGS-microstrip line combinations with frequency.

Table 4.3: Comparison of different unit cell of DGSs with the proposed unit cell of DGS

Parameter of DGS-microstrip line combination	**Different unit cell of DGS configurations**		
	Dumbbell-shaped [1–4]	**Fork-shaped [11]**	**Isosceles U-shaped [Proposed]**
Dimensions of single cell of DGS (mm)	a = 2, b = 1.9, g = 0.25	c = 1.05, d = 1, e = 0.5, f = 2.66, g_1 = 0.25	l_1 = 3.35, l_2 = 2.88, w = 0.25
Occupied defected ground area (mm^2)	8.475	3.765	2.1525
Quality factor	1.05	1.85	2.65
Resonating frequency f_0 (GHz)	15	15	15

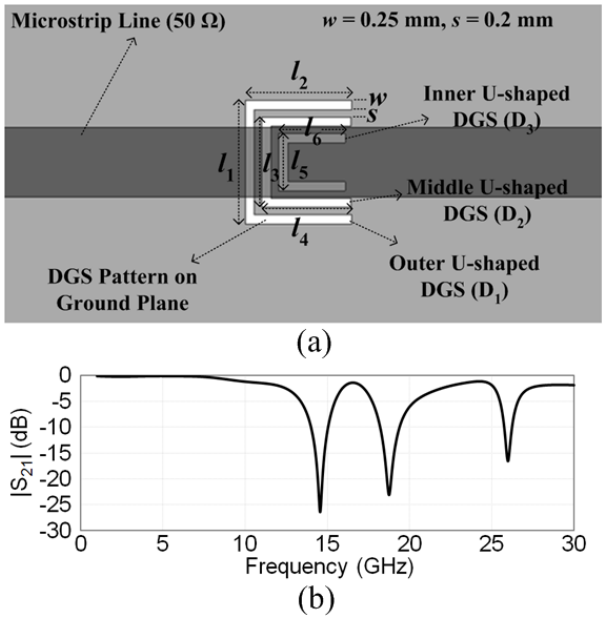

Figure 4.16: (a) Geometry of the proposed DGS unit-microstrip line combination. (b) Numerically simulated variation of $|S_{21}|$ of the proposed DGS unit-microstrip line combination with frequency.

4.4.3.2 Parametric Study

The dimensions of UDGSs play an important role in modifying the attenuation pole frequencies. In order to evaluate the effects of variations in dimensions of the proposed DGS unit on transmission coefficient $|S_{21}|$-frequency characteristic of DGS unit-microstrip line combination, the parametric study was performed through numerical simulation. Figure 4.17 depicts the variations of numerically simulated magnitude of S_{21} of the proposed DGS unit-microstrip line combination with frequency by taking 'l_2', 'l_4' and 'l_6' as parameters one at a time while keeping other parameters fixed. It can be observed from Figure 4.17 that significant variations in first, second and third attenuation pole frequencies are observed due to changes in side lengths 'l_2', 'l_4' and 'l_6' respectively. It can also be observed that little variation is observed in other attenuation pole frequencies due to change in side lengths $l_2/l_4/l_6$. This is due to the fact that larger side length(s) will have dominating effect on lower resonant frequency/frequencies of the structure.

4.4.3.3 Equivalent *RLC* Circuit Model

The equivalent *RLC* circuit model of the proposed DGS unit-microstrip line combination is shown in Figure 4.18. The modelling of the structure was done by considering each UDGS as a parallel *RLC* circuit. The coupling between UDGSs is represented through coupling capacitors C_{C12}, C_{C23}, and C_{C13}. The coupling capacitor between UDGSs D_1 and D_2 is represented by C_{C12}. Similarly, the coupling between UDGSs D_2 and D_3 is represented by the capacitor C_{C23} while that between UDGSs D_1 and D_3 is shown by capacitor C_{C13} in the equivalent circuit model. The *RLC* values and corresponding attenuation pole frequencies of different UDGS-microstrip line

combinations shown in Table 4.4 are calculated using Equation (4.5) by taking each UDGS separately.

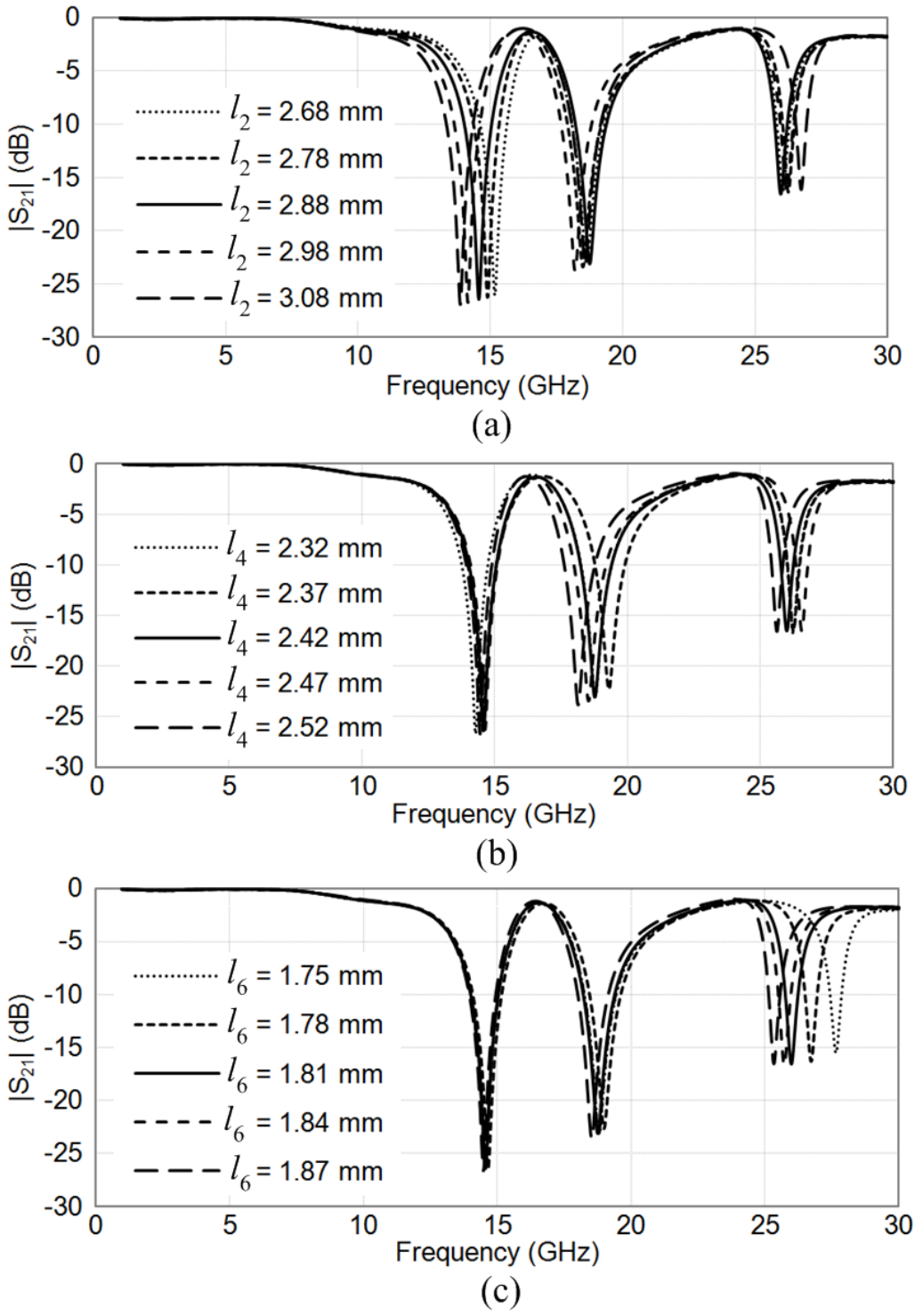

Figure 4.17: Variations of numerically simulated magnitude of S_{21} of triple isosceles UDGS (proposed DGS unit)-microstrip line combination with frequency for different values of (a) 'l_2', (b) 'l_4', and (c) 'l_6'; keeping other parameters fixed.

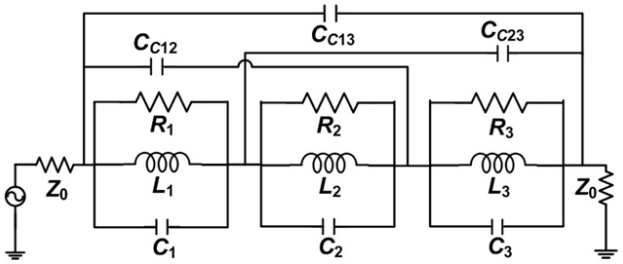

Figure 4.18: Equivalent circuit model of the proposed DGS unit-microstrip line combination.

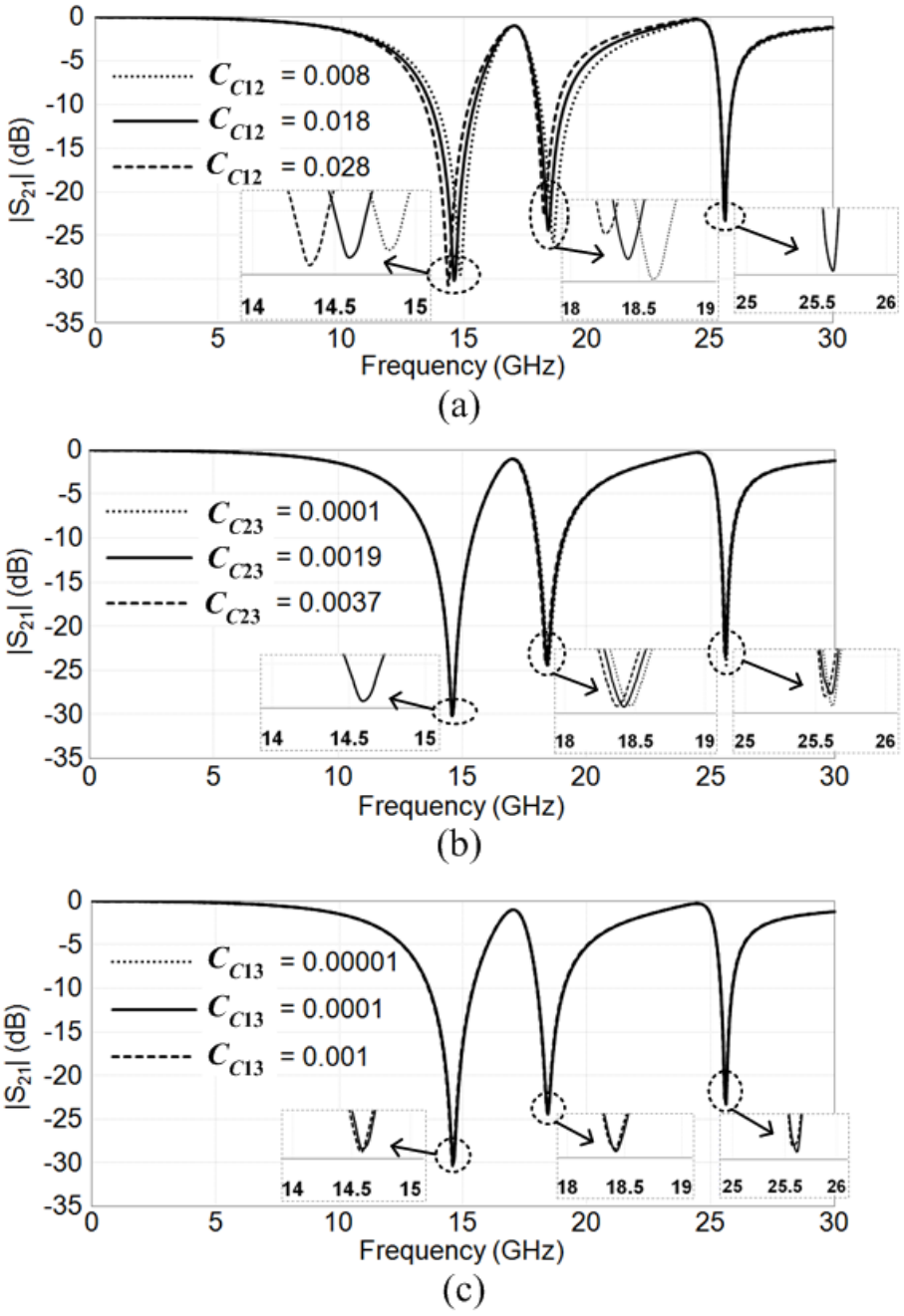

Figure 4.19: The $|S_{21}|$-frequency characteristics of the proposed DGS unit-microstrip line combination determined through circuit analysis for different values of coupling capacitor (a) C_{C12}, (b) C_{C23}, and (c) C_{C13}.

Table 4.4: Optimized dimensions of UDGSs and *R*, *L* and *C* values with resonant frequencies of their equivalent parallel resonant circuits.

Dimensions of DGS (mm); Resonant frequency (GHz)	**Resistance R_i (kΩ)**	**Inducatnce L_i (nH)**	**Capacitance C_i (pF)**
l_1 = 3.35, l_2 = 2.88; f_{01} = 15	R_1 = 2.7571	L_1 = 0.34297	C_1 = 0.32684
l_3 = 2.45, l_4 = 2.42; f_{02} = 18.86	R_2 = 2.143	L_2 = 0.1957	C_2 = 0.3641
l_5 = 1.55, l_6 = 1.81; f_{01} = 25.63	R_3 = 1.566	L_3 = 0.0329	C_3 = 1.1726

For quantification of coupling capacitors, initially the values of coupling capacitances which couple adjacent resonant circuits were chosen at most equal to 0.1 times of the value(s) of the capacitances of the associated resonant circuits. It is to be noted that coupling between distant DGSs and hence the value of coupling capacitor shunting two distant resonant circuits will be less than the coupling between adjacent DGSs and therefore the value of coupling capacitor shunting the adjacent circuits. Furthermore, to obtain final values of coupling capacitances in order to get theoretical results in conformity with the simulated ones, tuning was done through Computer Simulation Technology (CST) Design Studio software. To perceive the effect of coupling between UDGSs on the $|S_{21}|$-frequency characteristic of the DGS unit-microstrip line combination, coupling capacitors C_{C12}, C_{C23}, and C_{C13} were varied, and the results are shown in Figure 4.19. From Figure 4.19(a), it can be observed that variation in the value of C_{C12} brings about significant changes in first and second resonant frequencies while third attenuation pole frequency remains unaltered. This is because of less inter-DGS separation and larger dimensions of D_1 and D_2, the coupling between UDGSs D_1 and D_2 is higher which results in relatively larger value of coupling capacitor. It can be observed from Figure 4.19(b) that the second and third resonant frequencies of the UDGS unit are less affected due to variation in coupling capacitor

C_{C23} as compared with changes in first and second resonant frequencies of the structure owing to variation in C_{C12}. This happens because of smaller dimension of D_3 which results in lower coupling between UDGSs D_2 and D_3 and hence smaller value of C_{C23}. Similarly, Figure 4.19(c) shows that the effect of variation in the value of C_{C13} on the resonant frequencies of the UDGS unit is insignificant due to smaller dimensions of D_3 and the largest inter-DGS separation between D_1 and D_3 and hence the smallest value of capacitor C_{C13} among the coupling capacitors. Hence, by using coupled circuit analysis, the coupling capacitor values were optimised. The optimized values of coupling capacitors are: C_{C12} = 0.018 pF, C_{C23} = 0.0019 pF, and C_{C13} = 0.0001 pF.

4.4.3.4 Numerical and Circuit Simulation Results

Figure 4.20 shows the numerically simulated $|S_{21}|$-frequency characteristic and that obtained through circuit analysis for the proposed DGS unit-microstrip line combination. The $|S_{21}|$-frequency characteristic of the combination obtained through circuit analysis is nearly in agreement with numerically simulated one.

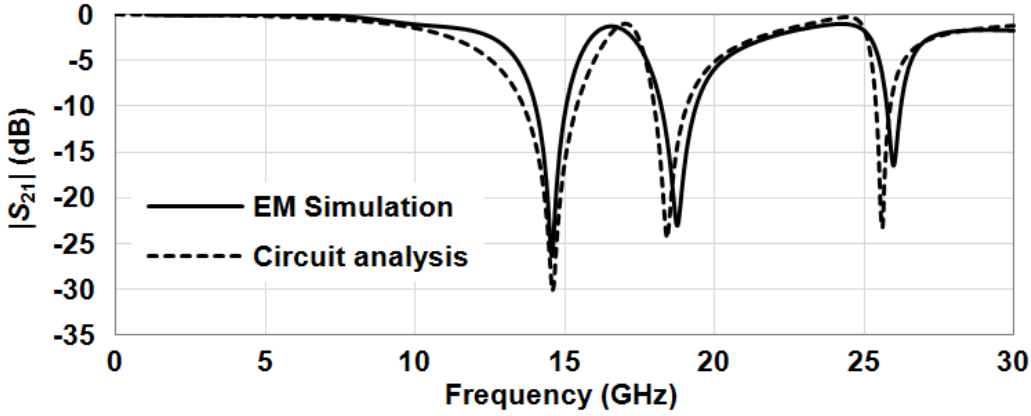

Figure 4.20: Variations of numerically simulated values of $|S_{21}|$ and those determined through circuit analysis for the proposed triple isosceles UDGS unit-microstrip line combination with frequency.

4.4.4 DGS-based LPF (the Proposed LPF)

4.4.4.1 Design of DGS-based LPF

To design the proposed compact LPF with wide stopband, non-uniform cascading of UDGSs has been considered. This is due to the fact that non-uniform configuration provides much wider stopband and small passband ripple simultaneously compared to the uniform configurations [Liu *et al*. (2004), Zhang and Mansour (2004), Ting *et al*. (2006)]. Figure 4.21 shows the geometry of the proposed LPF using four non-uniform cascaded triple isosceles UDGS units of optimized dimensions and inter-UDGS unit separation along with 50 Ω microstrip line. The optimised geometrical parameters of the proposed DGS-based LPF obtained through numerical simulation software are given in Table 4.5. The overall size of the defected ground is 14.44 mm × 3.4 mm. The dimensions of DGS units and spacing between them are optimized to obtain compact size LPF with desired performance. By considering different combinations of proposed DGS units of different dimensions and inter-DGS unit separations, it is found that four cascaded DGS units can provide the compact LPF with wide stopband. In the proposed LPF, four triple isosceles UDGS units are implemented to generate attenuation poles at the optimised frequencies (16.01 GHz, 21.63 GHz, 26.68 GHz), (17.52 GHz, 23 GHz, 27.23 GHz), (19.08 GHz, 24.27 GHz, 28.48 GHz), and (20.92 GHz, 25.62 GHz, 29.5 GHz) respectively to get wide stopband with compact size.

Further, to demonstrate the effectiveness of the proposed DGS-based LPF shown in Figure 4.21, two more DGS-based LPFs previously reported in the literature [Ahn *et al*. (2001), Lim *et al*. (2002), Ting *et al*. (2006)] were designed. First one designated as Type-I LPF (shown in Figure 4.22(a)) consists of a combination of 50 Ω microstrip line and four cascaded DGS units with each unit having double isosceles U-shaped DGSs while the second LPF designated as Type-II LPF (shown in Figure 4.22(b)) has a

combination of 50 Ω microstrip line and seven cascaded square dumbbell-shaped DGSs. The performance of the proposed LPF is compared with Type-I and Type-II LPFs. All these filters were designed for the same cut-off frequency of 14.2 GHz (cut-off frequency same as the proposed LPF) and are simulated on the Rogers RT/duroid 5880 substrate having dielectric constant (ε_r) of 2.2 and thickness of 0.787 mm. The overall size of the proposed filter, as well as Type-I and Type-II filters remains almost identical.

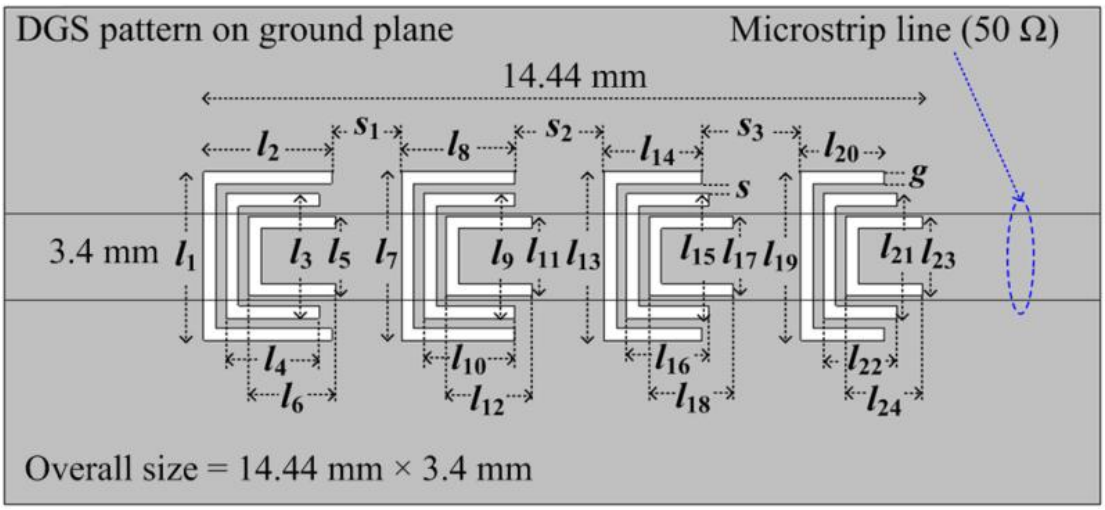

Figure 4.21: Geometry of the proposed DGS-based LPF using four cascaded triple isosceles UDGS units.

Table 4.5: Optimised parameters of DGS-based LPF (all dimensions are in millimeter)

l_1 = 3.4	l_2 = 2.57	l_3 = 2.5	l_4 = 1.87	l_5 = 1.6	l_6 = 1.74
l_7 = 3.4	l_8 = 2.27	l_9 = 2.5	l_{10} = 1.83	l_{11} = 1.6	l_{12} = 1.72
l_{13} = 3.4	l_{14} = 1.95	l_{15} = 2.5	l_{16} = 1.65	l_{17} = 1.6	l_{18} = 1.68
l_{19} = 3.4	l_{20} = 1.68	l_{21} = 2.5	l_{22} = 1.48	l_{23} = 1.6	l_{24} = 1.55
S = 0.2	g = 0.25	S_1 = 1.4	S_2 = 1.8	S_3 = 2	–

4.4.4.2 Numerical Simulation Study

The magnitudes of scattering parameters of the proposed LPF were determined at different frequencies through numerical simulation using Ansys HFSS software, and the simulation results are shown in Figure 4.23. It can be observed from Figure 4.23 that proposed LPF has simulated 3-dB cut-off frequency of 14.2 GHz with wide stopband up to 30 GHz. Of course, stopband can be extended beyond 30 GHz but at the cost of increased size. Therefore, there is a trade-off between size and performance of the LPF. The reflection coefficient in the passband of the proposed LPF is better than -10 dB. Further, the proposed LPF provides values of attenuation of at least 40 dB and 22 dB over the frequency ranges 15.4 – 21.8 GHz and 15.1 – 30 GHz respectively.

Figure 4.24 shows the numerically simulated variations of $|S_{21}|$ of the three DGS based LPFs (Proposed, Type-I, and Type-II) with frequency. All these filters exhibit similar passband response. Due to the existence of eight attenuation poles in Type-I filter, the stopband is achieved only up to about 24 GHz with minimum attenuation level of 20 dB. In case of Type-II filter, seven attenuation poles are generated due to the presence of seven DGSs, and stopband is achieved up to 25.5 GHz with minimum attenuation level of 20 dB. From Figure 4.24, it can be concluded that proposed filter has better response as compared with the previously reported DGS based LPFs. Further, the proposed LPF has slightly larger defected ground area as compared with Type-I LPF, but overall sizes of both LPFs are comparable. The stopband performance of the proposed filter is much better than Type-I and Type-II LPFs as shown in Figure 4.24. The defected ground area of the proposed LPF is found to be less as compared with Type-II LPF which would result in less radiation from ground plane in case of proposed LPF.

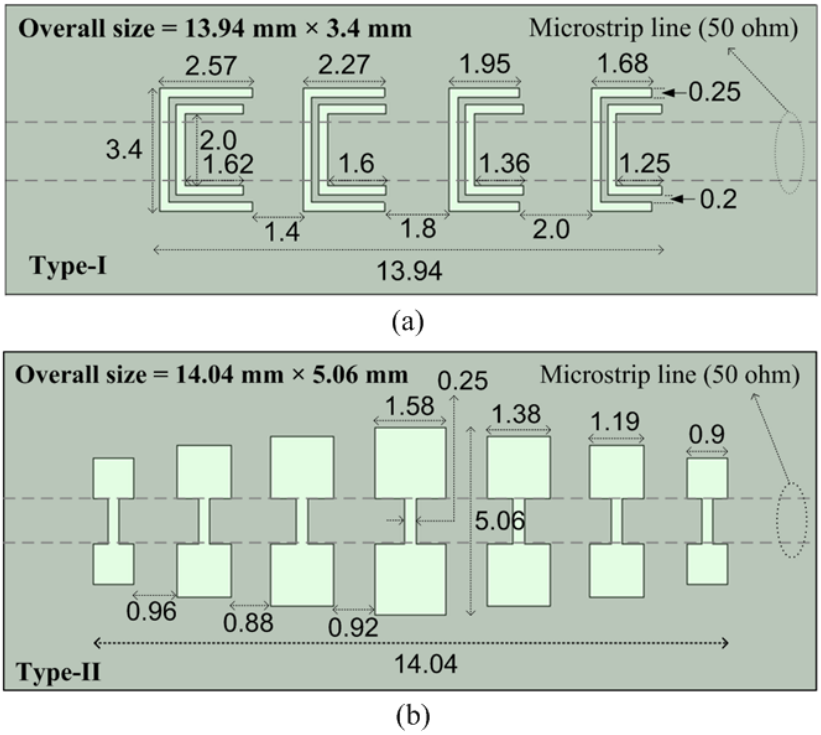

Figure 4.22: Geometries of LPFs using cascaded DGSs (a) Type-I, and (b) Type-II (all dimensions are in millimeter).

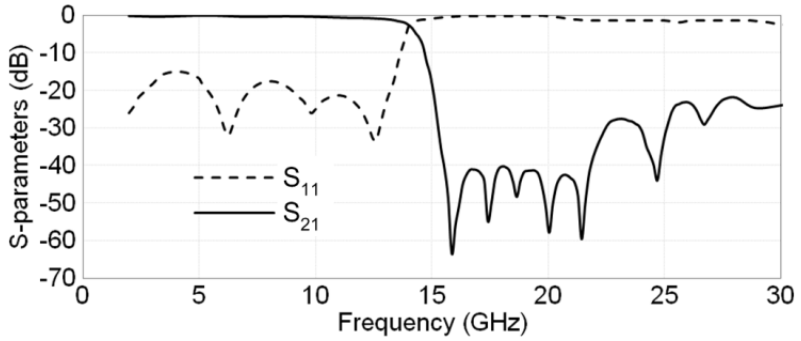

Figure 4.23: Numerically simulated variations of the magnitudes of *S*-parameters of the proposed LPF versus frequency.

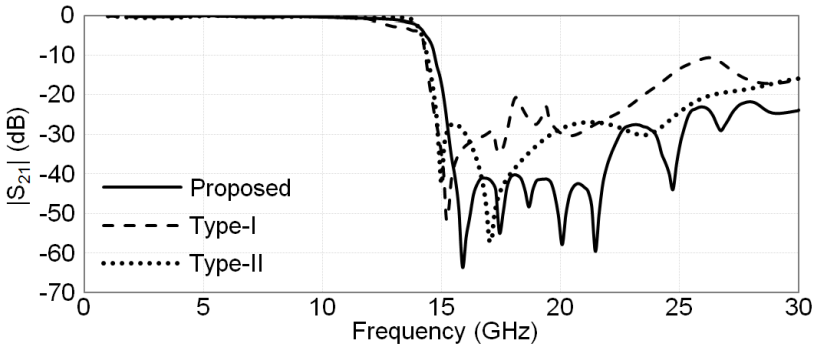

Figure 4.24: Numerically simulated variations of $|S_{21}|$ of the three DGS based LPFs (Proposed, Type-I, and Type-II) with frequency.

4.4.4.3 *RLC* Circuit Modelling and Analysis of the Proposed LPF

Figure 4.25 shows the equivalent *RLC* circuit model of the proposed LPF. The *RLC* model of each proposed DGS unit is cascaded through shunt capacitors [Ahn *et al*. (2001), Lim *et al*. (2002)] to obtain the equivalent circuit model of the proposed LPF. The *RLC* values of the proposed filter circuit computed using Equation (4.5) along with the attenuation pole frequencies of i^{th} UDGS (where i = 1–12) are shown in Table 4.6. The *RLC* values corresponding to attenuation pole frequencies (frequencies considered here are same as previously obtained during numerical simulation) are determined with the help of Equation (4.5). The couplings between UDGSs of DGS unit are represented through coupling capacitors C_{Cj12}, C_{Cj23}, and C_{Cj13}, where j = 1, 2, 3, and 4. The optimised values of coupling capacitors of the proposed equivalent circuit model of the proposed LPF are shown in Table 4.7. It is to be noted that coupling capacitors C_{Cj13} (j = 1, 2, 3, and 4) whose values are very small would not significantly affect the performance of the proposed LPF. Figure 4.26 shows variations of the magnitude of S-parameters of the proposed filter with frequency determined through circuit simulation. From Figure 4.26, it is found that the 3-dB cut-off frequency of the proposed filter found through circuit simulation is 13.8 GHz with wide stopband having attenuation level better than 48 dB over the frequency range 16.1 – 30 GHz.

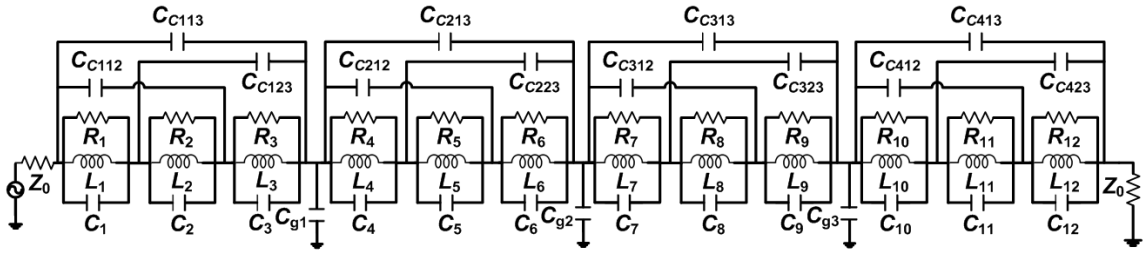

Figure 4.25: Equivalent *RLC* circuit model of the proposed LPF.

Table 4.6: *R*, *L*, and *C* values of the equivalent circuit model along with resonant frequency of i^{th} UDGS (where i = 1 – 12) for the proposed DGS-based LPF.

i	R_i (kΩ)	L_i (nH)	C_i (pF)	f_{0i} (GHz)
1	2.757	0.3001	0.2733	16.01
2	1.257	0.24355	0.2225	21.63
3	1.530	0.090199	0.39492	26.68
4	2.869	0.3498	0.23615	17.52
5	1.131	0.22818	0.21006	23
6	1.382	0.086058	0.39737	27.23
7	2.259	0.35286	0.19739	19.08
8	1.352	0.22254	0.19344	24.27
9	0.988	0.07474	0.41826	28.48
10	1.380	0.35057	0.16527	20.92
11	1.615	0.21729	0.17778	25.62
12	0.794	0.0758	0.38412	29.5

Table 4.7: Optimised coupling capacitor values for the equivalent circuit model of the proposed DGS-based LPF.

j	C_{Cj12} (pF)	C_{Cj23} (pF)	C_{Cj13} (pF)	C_{gj} (pF)
1	0.018	0.0019	0.0001	0.23
2	0.016	0.0016	0.0001	0.21
3	0.013	0.0014	0.0001	0.20
4	0.012	0.0012	0.0001	–

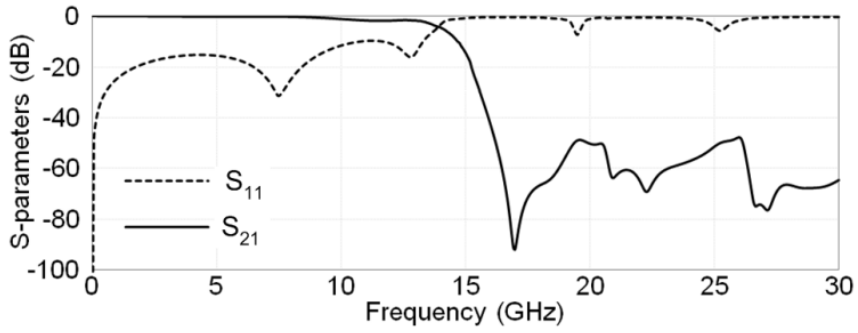

Figure 4.26: Variations of the magnitudes of *S*-parameters of the proposed LPF versus frequency determined through circuit simulation.

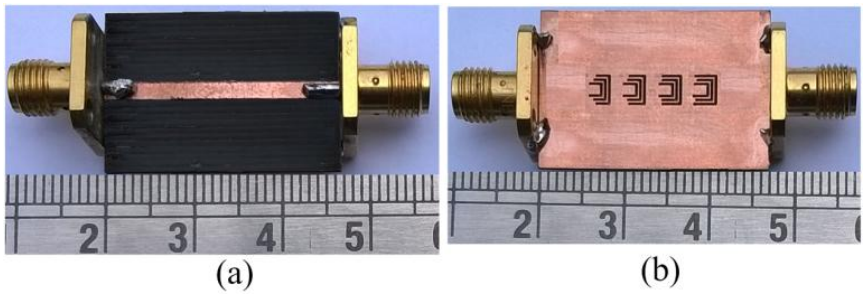

Figure 4.27: Fabricated prototype of the proposed LPF (a) Top view shows the 50 Ω microstrip conductor, and (b) Bottom view shows DGS pattern on the ground plane.

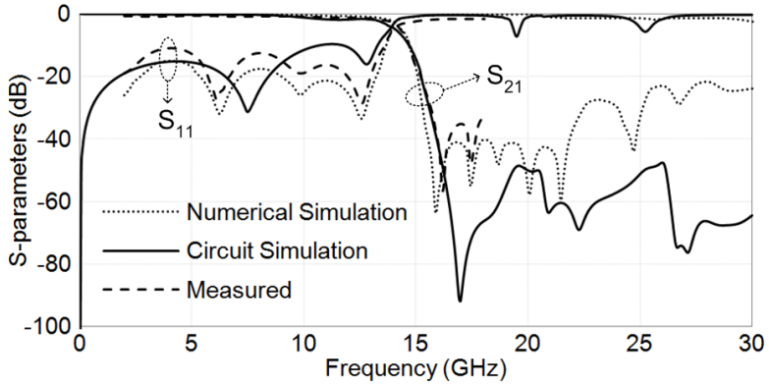

Figure 4.28: Variations of magnitude of S-parameters of the proposed LPF versus frequency obtained through numerical and circuit simulations as well as measurements.

4.4.4.4 Experiments, Results and Discussion for the Proposed LPF

The prototype of the proposed LPF was fabricated (shown in Figure 4.27) using T-Tech QC5000 prototyping system, and scattering parameters of the filter were measured at different frequencies using Agilent E8364B PNA network analyzer. The experimental results for the proposed filter are shown in Figure 4.28 along with numerical and circuit simulation results. Although the simulation study of the LPF was carried out up to 30 GHz, measurement was made up to 18 GHz only due to the limited operating frequency range of respective equipments/components available in the laboratory. The experimental results show that attenuation level in stopband is better than 34 dB over the frequency range 15.7–18 GHz. It can be seen from Figure 4.28 that experimental scattering parameter-frequency characteristics of the proposed LPF are nearly in

agreement with the respective numerical and circuit simulation characteristics in the frequency range of measurement. Also, it can be observed from Figure 4.28 that numerical and circuit simulation characteristics are also nearly in agreement with each other. The deviation in the results may be due to finite SMA connector losses, fabrication and measurement errors, and limitations of the equivalent circuit model of the filter.

Table 4.8: Comparison of the proposed filter with the LPFs reported in literature.

References	**Rectangular Size of defected ground (mm × mm)**	**Actual defected ground area (mm^2)**	**DC, H (mm)**	**Maximum Attenuation level, Stopband frequency range**	**f_c (GHz)**	**FC**
[Ting *et al*. (2006)]	70.68 × 13	207.97	3.38, 1.524	30 dB, 2.85 – 10 GHz	2.4	Simple
[Chen *et al*. (2009)]	16 × 14	36.94	3.2, 0.787	32 dB, 5.17 – 10 GHz	4.5	Complex
[Yu *et al*. (2009)]	13.5 × 11.1	41.475	3.48, 0.508	20 dB, 4.3 – 12.2 GHz	3.88	Simple
[Zhou *et al*. (2011)]	49 × 23	142.78	2.33, 0.79	20 dB, 2.1 – 8 GHz	1.84	Simple
[Liu *et al*. (2015)]	20.02 × 13.64	69.72	10.2, 0.635	25 dB, 3.24 – 10.7 GHz	3.11	Simple
[Fu and Yu (2016)]	16 × 8	36.96	3.55, 0.8	20 dB, 5.7 – 10 GHz	5.4	Simple
[Ertay *et al*. (2016)]	40 × 20	246.93	10.2, 1.27	20 dB, 1.65 – 7.41 GHz	1.49	Complex
[Vala *et al*. (2017)]	20 × 20	142	4.4, 1.2	12 dB, 4 – 10 GHz	3.5	Simple
Proposed work	**14.44 × 3.4**	**16.995**	**2.2, 0.787**	**40 dB, 15.4 – 21.8 GHz**	**14.2**	**Simple**
				22 dB, 15.1 – 30 GHz		

Note: In the Table 'DC', 'H', 'f_c', 'FC' stand for substrate dielectric constant, height of the substrate, 3 dB cut-off frequency and fabrication complexity respectively.

4.4.4.5 Performance Comparison of the Proposed LPF with the LPFs Reported in the Literature

Finally, performance and dimension based comparison of the proposed LPF with those reported in the literature with respect to rectangular defected ground size, actual defected ground area, out-of-band frequency range with rejection level, and fabrication complexity has been done, and the comparison data are presented in Table 4.8. It is apparent from Table 4.8 that the proposed filter is more compact in size, simple in fabrication and has wide stopband with good attenuation level. The proposed filter is simple in structure and does not employ compensated microstrip line, open stub, low-high impedance line, and tee- or cross-junction element reported in the literature. Because of simple structure, the proposed filter can be easily integrated with microwave systems. The proposed compact LPF having wide stopband can find potential applications in microwave systems in which harmonics and higher frequency interferences are to be suppressed.

4.5 Proposed UWB BPF (Modified MMR-based UWB BPF Integrated with DGS-based LPF)

4.5.1 Design and Investigation of the Proposed UWB BPF

It can be seen from Figure 4.11 that modified MMR-based UWB BPF provides spurious response at or near the frequency of 17 GHz. Therefore, in order to design the compact UWB BPF having passband of 3 – 11 GHz, wide stopband with high suppression capability and sharp roll-off, modified MMR-based UWB BPF is integrated with DGS-based LPF. The geometry of the proposed integrated design of filter is shown in Figure 4.29. The simulated variations of the magnitudes of S-parameters of modified MMR-based BPF directly integrated with DGS-based LPF without any alteration of

geometrical parameters are shown in Figure 4.30. From Figure 4.30, it can be observed that input impedance matching degrades significantly and insertion loss also degrades to small extent in passband of the filter. This is because of the loading effect of the DGS-based LPF circuit. Table 4.9 shows passband performance of the BPF before and after direct integration of the LPF. Further, it can also be observed from Figure 4.30 that the stopband performance of the filter (shown in Figure 4.29) is improved significantly due to integration of DGS-based LPF with modified MMR-based BPF. The loading effect of LPF circuit on the BPF circuit can be minimized or alternatively, the input impedance matching and insertion loss in the passband of the BPF–LPF combination can be improved through tuning of the circuit parameters i.e. by altering the geometrical parameters of the BPF–LPF combination using numerical simulation software. Better input impedance matching as well as improved insertion loss in passband and performance in stopband for the proposed filter are obtained by altering and optimizing the geometrical parameters of the BPF–LPF combination. Table 4.10 shows the optimised geometrical parameter values of the proposed filter. The simulation results of the proposed filter after optimization of geometrical parameters are shown in Figure 4.31. The simulated 3-dB bandwidth of the proposed filter covers the frequency range 3.0 – 11.0 GHz while corresponding insertion loss and group delay at mid-band frequency of UWB passband are 0.5 dB and 0.5 ns respectively. Upper stopband attenuation level of the proposed filter obtained through simulation is better than 40 dB and 25 dB over the frequency ranges 11.7 – 20.5 GHz and 11.2 – 30 GHz respectively. The roll-off (RO) rate ζ is defined as [Mirzaee and Virdee (2013)]

$$\zeta = \frac{\alpha_{\max} - \alpha_{\min}}{f_s - f_c} \quad \text{dB/GHz} \tag{4.6}$$

where α_{max} is the 20 dB attenuation point, α_{min} is the 3 dB attenuation point, f_s is the 20 dB stopband frequency and f_c is the 3 dB cutoff frequency. The roll-off rates in the lower and upper transition bands for the proposed filter are respectively equal to 18.7 and 54.8 dB/GHz. From the values of the roll-off rates, it can be concluded that the higher band-edge selectivity of the filter is better as compared to the lower band-edge selectivity.

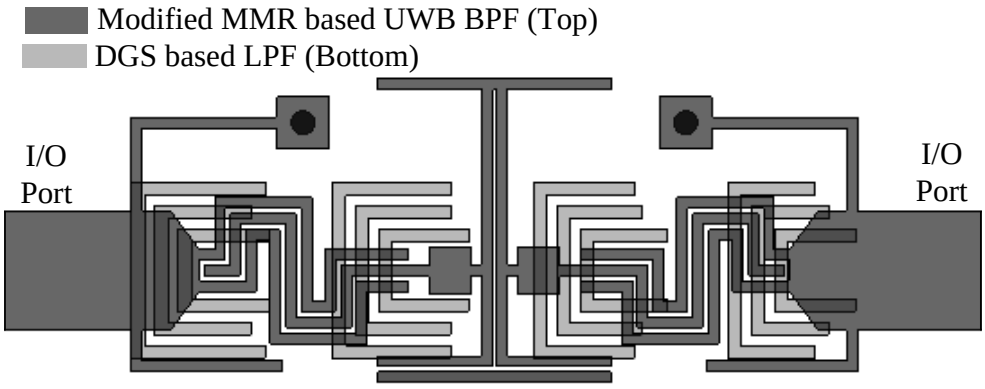

Figure 4.29: Geometry of the proposed compact UWB BPF.

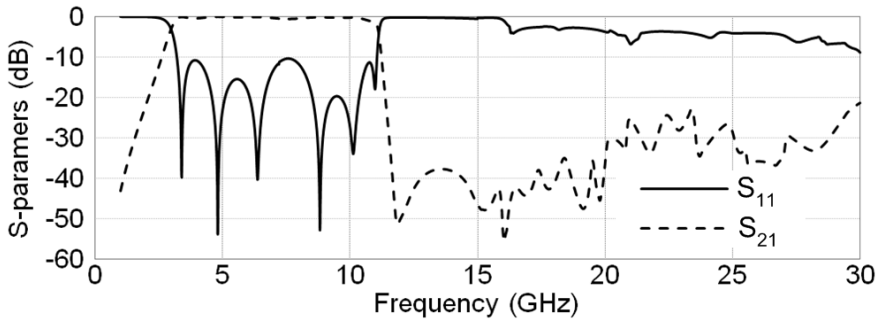

Figure 4.30: Variations of the magnitudes of S-parameters of the directly integrated BPF–LPF combination versus frequency obtained through numerical simulation.

Table 4.9: Simulation results of the BPF before and after integration of LPF.

	BPF before integration of LPF (shown in Figure 4.3)	BPF after integration of LPF (shown in Figure 4.23)
Highest reflection coefficient value in the passband	-13 dB	-10 dB
Maximum insertion loss in passband	0.5 dB	0.71 dB

Table 4.10: Optimised geometrical parameter values of the proposed filter (all dimensions are in millimeter)

$l'_1 = 0.53$	$l'_2 = 0.94$	$l'_3 = 1.12$	$l'_4 = 0.99$	$l'_5 = 0.25$	$l'_6 = 1.62$
$l'_7 = 0.35$	$l'_8 = 0.81$	$l'_9 = 0.2$	$l'_{10} = 0.91$	$l'_{11} = 1.53$	$l'_{12} = 3.38$
$l'_{13} = 1.0$	$l'_{14} = 0.46$	$l'_{15} = 2.69$	$l'_{16} = 1.8$	$l'_{17} = 0.83$	$l'_{18} = 2.75$
$l'_{19} = 1.99$	$l'_{20} = 2.02$	$g' = 0.11$	$w' = 0.2$	$l_1 = 3.4$	$l_2 = 2.57$
$l_3 = 2.49$	$l_4 = 1.87$	$l_5 = 1.61$	$l_6 = 1.74$	$l_7 = 3.42$	$l_8 = 2.28$
$l_9 = 2.49$	$l_{10} = 1.83$	$l_{11} = 1.61$	$l_{12} = 1.72$	$l_{13} = 3.41$	$l_{14} = 1.95$
$l_{15} = 2.51$	$l_{16} = 1.66$	$l_{17} = 1.61$	$l_{18} = 1.72$	$l_{19} = 3.4$	$l_{20} = 1.68$
$l_{21} = 2.51$	$l_{22} = 1.47$	$l_{23} = 1.61$	$l_{24} = 1.54$	$S = 0.2$	$g = 0.25$
$S_1 = 1.28$	$S_2 = 1.60$	$S_3 = 1.77$	–	–	–

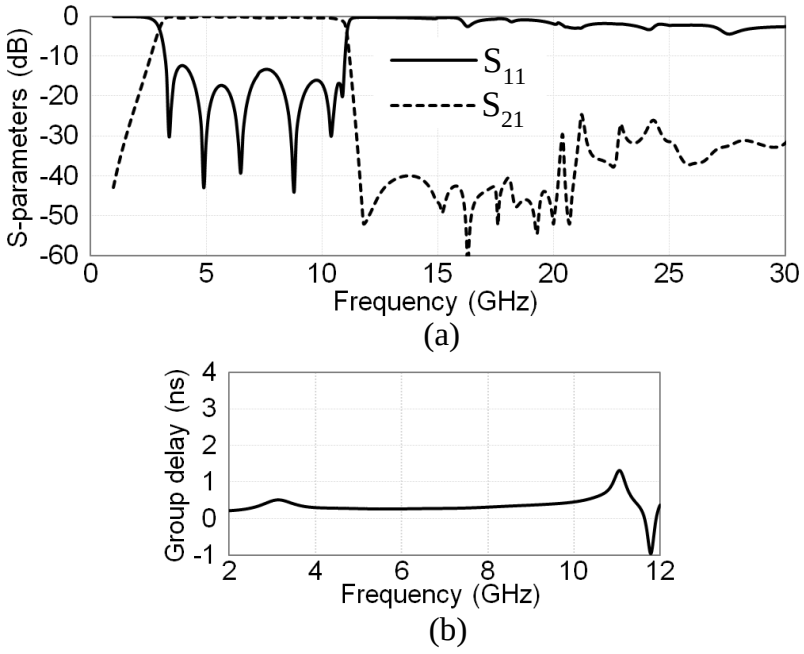

Figure 4.31: Simulation results for the proposed filter (a) S-parameter-frequency characteristics, and (b) Group delay-frequency characteristic.

4.5.2 Equivalent Circuit Model of the Proposed UWB BPF

The equivalent circuit model of the proposed UWB BPF is obtained through cascading of the equivalent circuit model of the modified MMR-based UWB BPF with the equivalent circuit model of the DGS-based LPF. Figure 4.32 shows the equivalent

circuit model of the proposed UWB BPF. The cascading of equivalent circuit models is done by using a coupling capacitor C_{c4} . The reactance of coupling capacitor C_{c4} should be much lower as compared to input impedance of the LPF for lowest frequency of operation of the BPF.

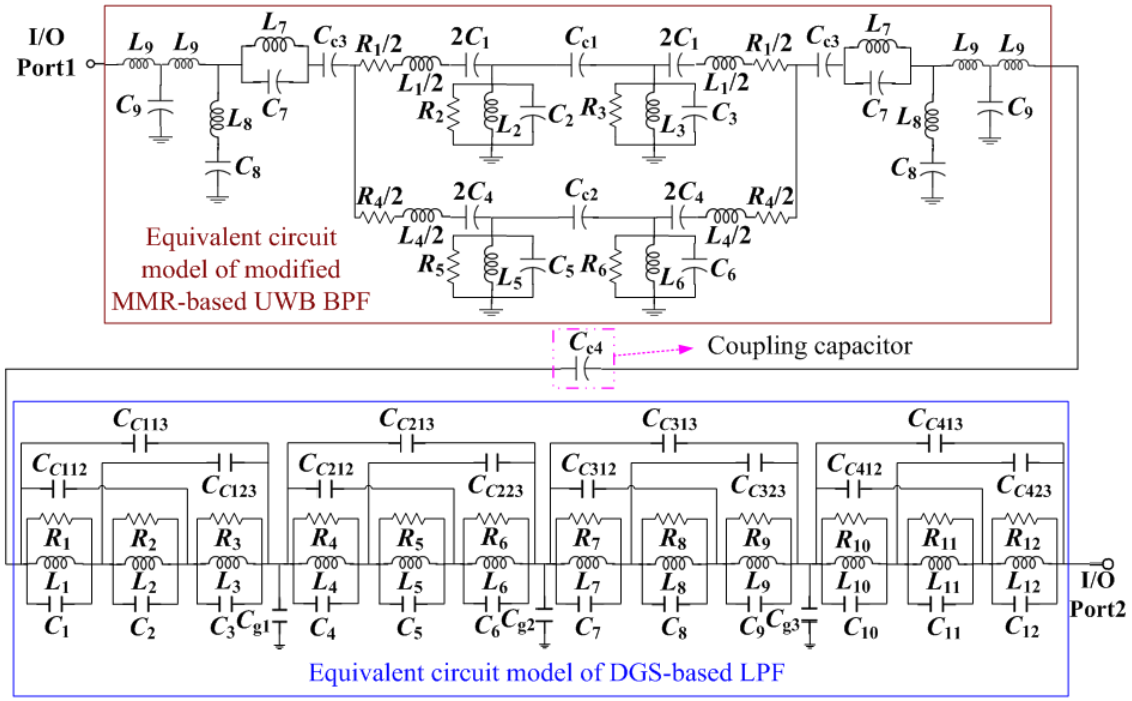

Figure 4.32: Equivalent circuit model of the proposed UWB BPF.

4.5.3 Simulated Surface Current Distributions

To better understand the usefulness of DGS-based LPF for suppression of out-of-band harmonics for obtaining wide stopband, the current distributions on the surfaces of the proposed compact UWB BPF are discussed by considering the filter structure with and without DGS-based LPF. Figure 4.33 depicts the surface current distributions on top and bottom surfaces of the proposed filter with and without DGS-based LPF at a frequency of 16.7 GHz (a simulated frequency where undesired response is obtained without DGSs). It can be noticed from Figure 4.33 (a) that higher level of current reaches port 2 from port 1 through ground plane in the absence of DGS units. Therefore,

in order to obtain wide stopband, DGS-based LPF was used to block the passage of current from port 1 to port 2. It can be clearly observed from Figure 4.33 (b) that in the presence of DGS units, most of the current is concentrated near the boundaries of the DGSs, which are responsible for providing high attenuation at or near the frequency of 16.7 GHz and almost negligible current reaches port 2 from port 1 of the filter.

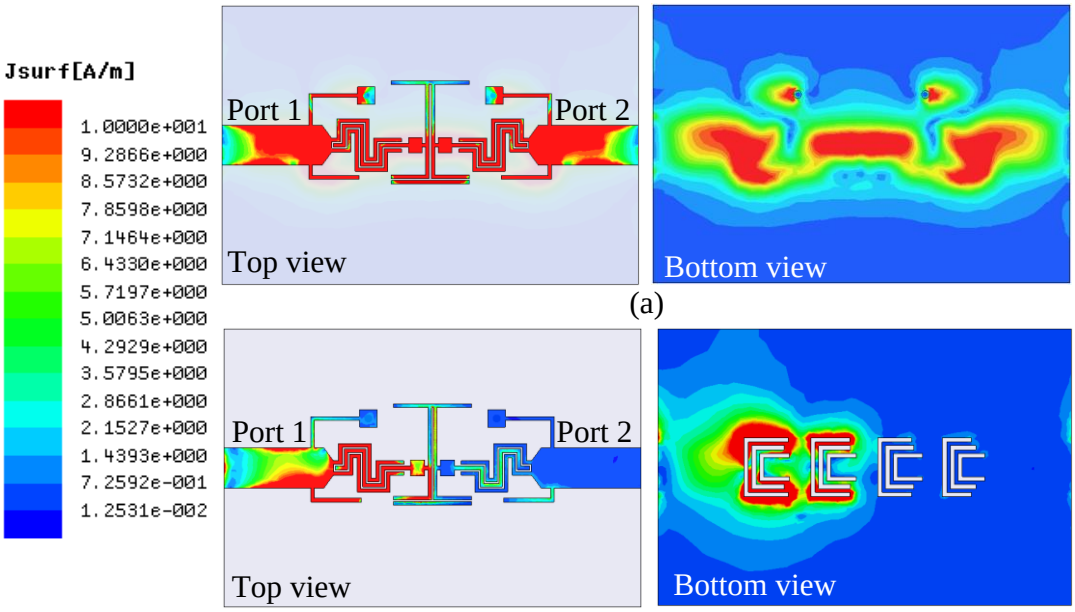

Figure 4.33: Simulated surface current distributions of the proposed filter at a frequency of 16.7 GHz (undesired response frequency without DGSs) (a) Without DGS-based LPF, and (b) With DGS-based LPF.

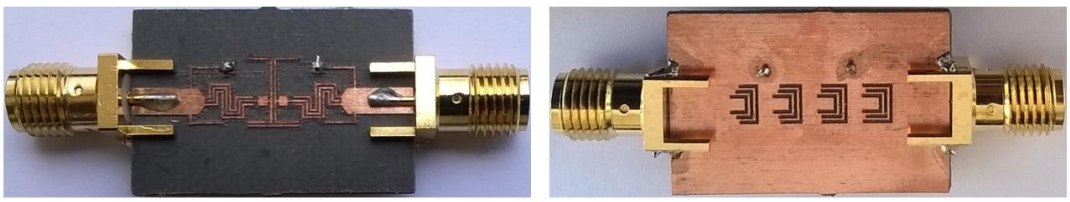

Figure 4.34: Fabricated prototype of the proposed filter (a) Top view, and (b) Bottom view.

4.5.4 Experiments, Results and Discussion

The prototype of the proposed filter was fabricated (shown in Figure 4.34) on RT/duroid 5880 substrate (ε_r = 2.2, tanδ = 0.0009 and thickness = 0.787 mm) using T-

Tech QC5000 prototyping system and parameters of interest at different frequencies are measured using Agilent E8364B PNA network analyzer. The experimental results for the proposed filter are shown in Figure 4.35 along with numerical simulation results. Although the simulation studies of the filter were performed up to 30 GHz, measurement was made up to 18 GHz only due to limited operating frequency range of respective equipments/components available in the laboratory. The simulation and experimental results for the proposed filter are shown in Figure 4.35. The simulated (measured) 3-dB bandwidth covers the frequency range 3.0 – 11.0 GHz (3.05 – 10.9 GHz) while corresponding insertion loss and group delay at mid-band frequency of filter UWB passband are 0.5 dB (0.9 dB) and 0.5 ns (0.9 ns) respectively. Upper stopband attenuation level obtained through simulation (measurement) is better than 40 dB (37.8 dB) up to 18 GHz. The experimental results of the proposed filter are nearly in agreement with the respective simulation results. The deviation in the results may be due to finite SMA connector losses, as well as fabrication and measurement errors.

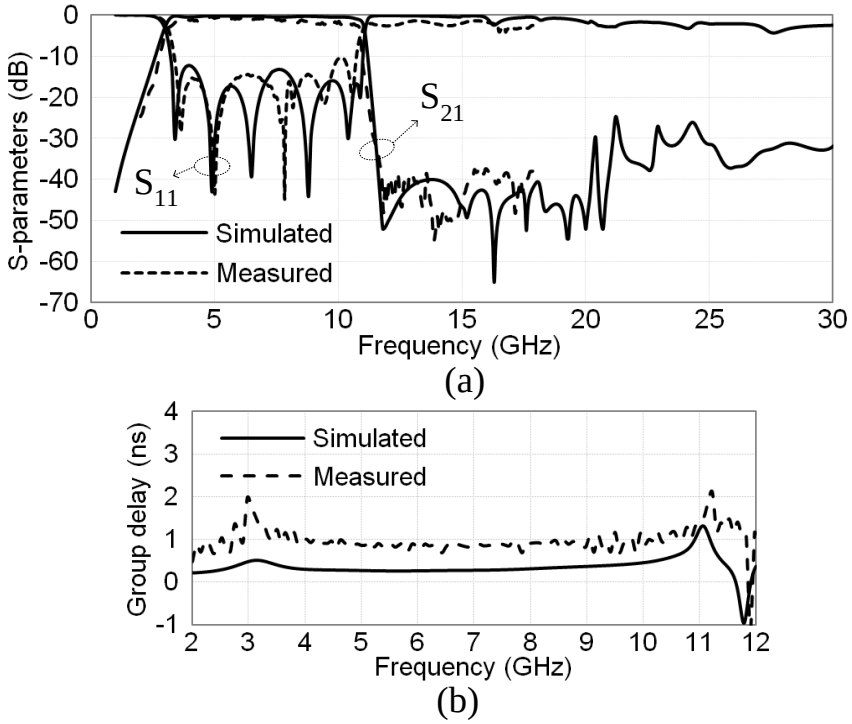

Figure 4.35: Simulation and measured results for the proposed filter (a) S-parameter-frequency characteristics, and (b) Group delay-frequency characteristics.

Table 4.11: Performance comparison of the proposed UWB BPF with those reported in the literature.

Reference	**3-dB bandwidth (GHz)**	**Stopband upto the frequency (GHz), minimum attenuation (dB)**	**Size (mm × mm)**	**Substrate dielectric constant, and height (mm)**
[Wong and Zhu (2007)]	3.4–11	20, 15	12.5 × 2.0	10.8, 0.635
[Yang *et al*. (2007)]	3.0–10.8	20, 20	20 × 50	2.65, 1.0
[Gong *et al*. (2008)]	2.9–10.7	19.1, 20	33 × 15	2.55, 0.8
[Yao *et al*. (2009)]	2.8–10.6	27.8, 30	13.6 × 2.8	10.8, 0.635
[Chu *et al*. (2011)]	3.1–11.1	17.1, 20	22.5 × 13.7	2.55, 0.8
[Yang *et al*. (2011)]	3.0–10.3	14, 30	16.5 × 16.5	2.2, 0.508
[Ghatak *et al*. (2011)]	2.9–11.6	20, 25	27 × 22	2.2, 0.787
[Sarkar *et al*. (2012)]	3.15–10.62	25, 20	22 × 10	2.2, 0.787
[Taibi *et al*. (2015)]	3.2–11.1	17.6, 20	16.7 × 13.4	2.33, 0.5
[Li *et al*. (2015)]	3.4–10.7	17, 38	22 × 5.3	2.2, 0.508
[Jhariya *et al*. (2015)]	3.75–13.75	19, 16	15 × 4	4.4, 1.6
[Kumar *et al*. (2016)]	3.09–10.62	17.1, 20	32.4 × 26.7	2.33, 0.79
[Zhang *et al*. (2016)]	3.2–11.2	16, 30	20.3 × 5.3	2.2, 0.508
Proposed work	**3.0–11.0**	**20.5, 40 and 30, 25**	**14 × 5.9**	**2.2, 0.787**

4.5.5 Performance Comparison of the Proposed UWB BPF with the BPFs Reported in the Literature

Finally, performance comparison of the proposed filter with others reported in the literature is given in Table 4.11. It is apparent from Table 4.11 that the proposed filter is more compact and provides good out-of-band suppression as compared with the filters reported in the literature.

4.6 Conclusion

In this chapter, study of compact UWB BPF with wide stopband has been described which utilizes modified MMR-based UWB BPF structure in combination with DGS-based LPF configuration. The meandered coupled-lines, stepped-impedances stubs, open- and short-circuited stubs of the modified MMR-based UWB BPF are responsible for significant reduction in size with good impedance matching in passband of the proposed filter. Four non-uniform configurations of DGS units have been utilized to obtain compact LPF. Wide stopband for the LPF has been obtained using twelve attenuation poles corresponding to four DGS units without increasing the overall size of the filter. The proposed DGS-based LPF has been analysed through equivalent *RLC* circuit model. The circuit simulation results of LPF are nearly in agreement with corresponding numerical simulation and measured results. Finally, DGS-based LPF has been integrated with modified MMR-based UWB BPF resulting in compact UWB BPF with wide stopband. Further, proposed filter was fabricated and parameters of interest were measured to validate the corresponding numerical simulation results. The proposed compact filter with good passband characteristics and improved out-of-band performance can be used as an important component/device in modern UWB communication system and in portable UWB systems.

In the next chapter, a new compact UWB filtering antenna is proposed. The proposed compact UWB filtering antenna is obtained through integration of a new UWB monopole antenna with the compact UWB BPF, which is investigated in the present chapter.